Mathematical Medicine and Biology (2004) **21**, 293–334

Platelet–wall interactions in continuum models of platelet thrombosis: formulation and numerical solution

AARON L. FOGELSON†
Departments of Mathematics and Bioengineering, University of Utah, Salt Lake City, Utah 84112, USA

AND

ROBERT D. GUY
Department of Mathematics, University of Utah, Salt Lake City, Utah 84112, USA

[Received on 25 March 2004; revised on 11 June 2004]

A model is developed to describe the formation of platelet thrombi in coronary-artery-sized blood vessels. It involves interactions among a viscous, incompressible fluid; populations of non-activated and activated platelets; activating chemicals; and the vessel walls. Adhesion of platelets to the injured wall and cohesion between activated platelets is modelled using distributions of elastic links which generate stresses that can influence the fluid motion. The first version of the model presented involves two spatial scales: the microscale of the platelets and the macroscale of the vessel. A closure approximation is introduced that allows essential microscale behaviour to be computed while eliminating the necessity to explicitly track events on this scale. Computational methods are presented that meet the diverse challenges posed by the coupled nonlinear partial differential equations of the model and by the complex geometry of the constricted vessels in which the thrombosis simulations are carried out. Simulation results demonstrate that the model can produce thrombi that grow to occlude the vessel, that shear-stress exerted by the fluid on the thrombi can modify their subsequent growth and cause remodelling of their shape through small-scale local changes or large-scale structural breakup.

Keywords: blood clotting; platelet aggregation; immersed boundary; immersed interface; multiscale modelling; biofluid dynamics.

1. Introduction

Platelet aggregation is a principal component of the blood clotting response, and thus plays a major role in normal hemostasis as well as in the pathological thrombosis that is responsible for many severe cardiovascular problems. In Fogelson (1992, 1993) we began development of continuum models of platelet aggregation aimed at studies of this process in blood vessels the size of coronary arteries or larger. These are the vessels of greatest clinical interest because of the serious consequences if they are blocked. The models presented in these papers described aggregation only in the solution-phase of the flowing blood; no interactions between platelets and the blood vessel walls were included. Since these platelet–wall interactions are critical to the initiation of aggregation, and since

†Email: fogelson@math.utah.edu

it is the adhesion of platelets to portions of the wall that holds the aggregates in place, it is important to extend these models to incorporate such interactions. The purpose of this paper is to describe how platelet–wall interactions can be included in the continuum models of aggregation, to describe numerical methods for solving the resulting equations, and to present our initial explorations of these more complete aggregation models.

When a blood vessel is injured, platelets suspended in the blood adhere to the damaged tissue. Other platelets adhere to these wall-adherent platelets and cohere with one another to form a loose 'platelet plug' or aggregate that fills the hole and stems the loss of cellular elements in the blood (most importantly, the oxygen-carrying red blood cells). This is the role platelets play in normal hemostasis (Weiss, 1975). Similar events can be triggered by pathologies of the vessel wall, and can lead to the growth of aggregates that occlude the vessel and prevent oxygen from reaching tissue normally supplied by the blood vessel. This pathological aggregation is referred to as thrombosis, and the resulting aggregate is called a thrombus (*pl.* thrombi). One situation in which this happens and which is very important clinically is associated with atherosclerosis (Forrester *et al.*, 1987; Fuster *et al.*, 1988). Over the course of many years, atherosclerotic plaques can grow on the inner wall of a coronary artery to the point where 80–90% of the vessel lumen is occluded. The plaque material is fragile and easily ruptured by hemodynamic stresses. When a plaque ruptures, platelet reactive material is exposed, and a platelet thrombus quickly forms at the site of rupture. This acute thrombotic event can lead to complete blockage of the vessel, and such events are believed to be the proximal cause of a substantial fraction of myocardial infarcts. Pathological thrombi also form in association with blood-contacting prosthetic devices like vascular grafts and artificial cardiac valves (Cannegieter *et al.*, 1994). In all of these situations, there are strong suggestions from clinical data and experimental results that the local fluid dynamics of the blood, influenced by the local geometry of the vessel or prosthetic device, plays an important role in determining the rate and final extent of aggregate growth (Grabowski *et al.*, 1978, 1972; Turitto & Baumgartner, 1975; Turitto & Weiss, 1979). A long-term goal of our work towards which the present paper contributes is to better understand the interactions between local geometry, fluid dynamics, and aggregate growth.

Platelets are non-nucleated cells suspended in the blood plasma. In a healthy person, there are approximately 250 000 platelets per mm^3 of blood. Yet because of their small size, platelets occupy less than 0·3% of the blood's volume. Platelets normally circulate in a dormant or unactivated state in which they do not adhere either to other platelets or to the intact blood vessel wall. A variety of plasma-borne chemical stimuli, including adenosine diphosphate (ADP) and the enzyme thrombin, can bind to specific receptors on the platelet's surface (Andersen *et al.*, 1999; Andre *et al.*, 2003; Clemetson, 1995; Dorsam & Kunapuli, 2004) and thereby trigger the platelet *activation* process. Shear stresses above those encountered in healthy individuals can also activate platelets through a mechanism that seems to depend on large von Willebrand factor multimers attached to the platelet surface (Moake *et al.*, 1988). Platelet activation entails (i) the platelet's surface membrane becoming sticky to other activated platelets; (ii) the platelet beginning to release platelet-stimulating chemicals into the surrounding plasma; and (iii) the platelet changing morphologically from its rigid discoidal resting shape, to a more deformable approximately spherical form from which extend several long thin appendages known as pseudopodia (Weiss, 1975). The change that makes the platelet's surface membrane

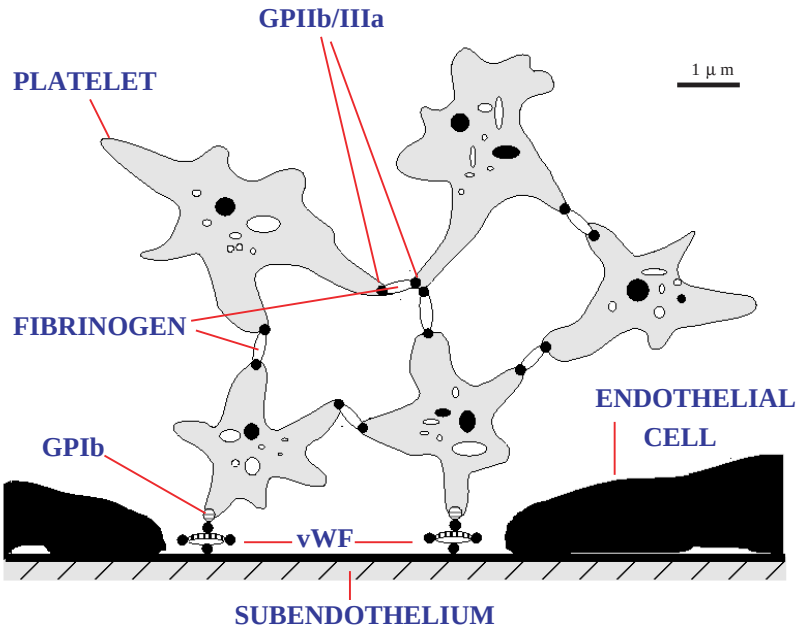

FIG. 1. Schematic illustration of platelet adhesion and aggregation.

sticky is the expression of surface receptors (GP-IIb/IIIa receptors) for the plasma protein fibrinogen. Fibrinogen is a dimeric protein that can bind to one such receptor on each of two activated platelets to form a molecular bond between the platelets (See Fig. 1). Each platelet has approximately 50 000 GP-IIb/IIIa receptors and this allows the possibility of numerous such fibrinogen bridges between a pair of coherent platelets (Marguerie *et al.*, 1986). The surface of an activated platelet changes in other ways which allows it to take part in the enzyme reactions which comprise the blood coagulation process. In particular, the coagulation enzyme thrombin is synthesized on the surface of an activated platelet and then dissociates into the surrounding blood plasma (Kuharsky & Fogelson, 2001; Mann & Lorand, 1993). Activated platelets also release ADP from cytoplasmic storage granules into the surrounding plasma (Lages, 1986). Both thrombin and ADP are potent platelet activators; their relative importance for *in vivo* aggregation is not known. Since both ADP and thrombin cause platelet activation and are released by activated platelets, the aggregation process involves positive feedback loops. The shape changes that platelets undergo upon activation are believed to be quite important to aggregate formation: the pseudopodial extensions are thought to promote platelet–platelet contact, and the deformability of activated platelets allows their surface membranes to come into close apposition which permits enhanced formation of fibrinogen bridges and thus stronger cohesion (White, 1994). The shape change is at a scale that is not directly relevant to the models that will be discussed below.

Since platelet aggregation has the potential for positive reinforcement it is important that regulatory mechanisms exist to prevent its initiation when it is not needed, and to limit its spatial extent when it does occur. A healthy intact blood vessel is lined by a confluent monolayer of endothelial cells that present a very smooth surface to the passing blood. These cells actively work to prevent the initiation of aggregation, in part by the production and release into the plasma of prostacyclin which is a potent platelet inhibitor, and by the activity of molecules on their luminal surfaces that neutralize thrombin and degrade ADP (Esmon, 1992; Marcus & Safier, 1993). Because of these activities, the luminal surface of healthy endothelial cells is very thromboresistant. The endothelial cells also produce a molecule called von Willebrand factor (vWF), important for platelet adhesion, which is released into the plasma from the endothelial cells' luminal side, and onto the subendothelial extracellular matrix on the endothelial cells' abluminal side. The surface of a platelet, non-activated or activated, displays GP-Ib molecules which can bind to vWF, but the binding site on vWF for GP-Ib is hidden unless the vWF is in the presence of collagen from the subendothelial matrix. So the vWF released into the plasma does not normally cause platelet adhesion, but if the endothelial cells are disrupted, the vWF bound to collagen on the subendothelial matrix is ready to bind to platelet GP-Ib. This leads directly to platelet adhesion to the subendothelial matrix, and furthermore, the binding of vWF to GP-Ib results in an intraplatelet signal that causes activation of that platelet. (See Mohammad, 1995; Ruggeri, 1997 for further discussion.)

For platelets to adhere to damaged vessel tissue, the platelets must, of course, contact that tissue. Thus transport of platelets to this tissue by advection and diffusion is critical to the aggregation process. The duration of platelet and activating chemical proximity to the damaged tissue is also important, and there is experimental evidence that suggests that entrapment of platelets and chemicals in recirculation zones near protruding atherosclerotic plaques, and near bends and branchings of blood vessels, may be associated with higher incidences of thrombosis at such sites (Badimon & Badimon, 1989; Barstad *et al.*, 1994; Karino & Goldsmith, 1980; Karino & Motomiya, 1984). Another way that fluid dynamics may affect aggregate growth is that sufficiently high fluid stresses on an aggregate surface may make it impossible for new platelets to remain attached to the aggregate. Similarly, fluid stresses can dislodge portions of an existing aggregate by breaking the bonds between platelets in the aggregate. This is known as embolization and is important clinically because emboli can block smaller vessels downstream of the site from which they were detached. As already indicated above, aggregate growth can profoundly affect the flow of the blood, to the point that complete occlusion of a vessel prevents flow entirely. The two-way coupling between fluid dynamics and aggregate growth makes studying aggregation challenging and interesting.

The outline of the remainder of this paper is as follows. In Section 2, we review the solution-phase aggregation models presented in Fogelson (1992, 1993). In Section 3, we introduce an extension of the solution-phase model that allows us to study embolization. In Section 4, we introduce the additional variables and equations we use to model platelet interactions with the vessel walls and other reactive surfaces. In Section 5, we describe the computational methods that are used to solve the model's equations, and in Section 6, we describe some results from computational studies of the model.

2. Review of solution-phase aggregation models

The models of platelet aggregation introduced in Fogelson (1992, 1993) involve interactions among a viscous, incompressible fluid; populations of non-activated and activated platelets; a population of interplatelet elastic links; and a platelet-activating chemical. The activating chemical acts on non-activated platelets to produce activated platelets. Activated platelets interact with one another to produce interplatelet elastic links. The links can be stretched by gradients in the fluid velocity and then produce stresses that affect the fluid. These stresses are the only way that the platelets influence the fluid dynamics.

The problem that the models address involves two distinct length scales; the diameter of a coronary artery is on the order of 1 mm, and the diameter of a platelet is about 1 μm. Because of this, two sets of spatial variables appear in the final models; these are $\mathbf{x}$ and $\mathbf{y}$ for which the statements $|\mathbf{x}| = \mathrm{O}(1)$ and $|\mathbf{y}| = \mathrm{O}(1)$ indicate lengths comparable to a vessel diameter or platelet diameter respectively. We denote by ϵ the ratio of platelet diameter to vessel diameter and note that $\epsilon \ll 1$. The equations of the continuum model are the leading order terms for the limit of small ϵ.

For a variety of reasons, it is desirable to use a different scaling of the model variables than used in the original aggregation papers. Other than the scaling, the models are mathematically equivalent. In the scalings and notation we use in this paper, we let $\mathbf{u}(\mathbf{x}, t)$ and $p(\mathbf{x}, t)$ denote the fluid velocity and pressure; $\phi_{\mathrm{n}}(\mathbf{x}, t)$ and $\phi_{\mathrm{a}}(\mathbf{x}, t)$ be the non-activated and activated platelet concentration respectively, and $c(\mathbf{x}, t)$ be the concentration of activating chemical. We use $z^{\mathrm{p}}(\mathbf{x}, t)$ to denote the concentration of elastic links between activated platelets at $\mathbf{x}$ and activated platelets elsewhere. We define a function $\widetilde{E}(\mathbf{x}, \mathbf{r}, t)$ so that $\widetilde{E}(\mathbf{x}, \mathbf{r}, t)\,\mathrm{d}\mathbf{r}$ is the concentration of elastic links between activated platelets at $\mathbf{x}$ and activated platelets in a small volume around $\mathbf{x} + \mathbf{r}$. It then follows that

$$z^{\mathrm{p}}(\mathbf{x}, t) = \int \widetilde{E}(\mathbf{x}, \mathbf{r}, t)\,\mathrm{d}\mathbf{r}. \tag{2.1}$$

The function $\widetilde{E}$ has dimensions of number of elastic links per volume ($\mathbf{x}$) per volume ($\mathbf{r}$). The variable z^{p} plays a more prominent role in the current models than previously and this is one reason for the new scaling. The platelet length scale is much smaller than the macroscopic length scale and so we expect $\widetilde{E}$ to vary rapidly with the separation vector $\mathbf{r}$. Because of this, we make a change of variables $\mathbf{r} = \epsilon\mathbf{y}$, and we define $E(\mathbf{x}, \mathbf{y}, t) = \epsilon^3\widetilde{E}(\mathbf{x}, \mathbf{r}, t)$ so that $z^{\mathrm{p}}(\mathbf{x}, t) = \int E(\mathbf{x}, \mathbf{y}, t)\,\mathrm{d}\mathbf{y}$. The functions $\mathbf{u}$, p, ϕ_{n}, ϕ_{a}, c, and E are the basic unknowns of the model.

The most general form of the solution-phase aggregation models is as follows:

$$\rho(\mathbf{u}_t + \mathbf{u}\cdot\nabla\mathbf{u}) = -\nabla p + \mu\Delta\mathbf{u} + \mathbf{f} \tag{2.2}$$

$$\nabla\cdot\mathbf{u} = 0 \tag{2.3}$$

$$\frac{\partial\phi_{\mathrm{n}}}{\partial t} + \mathbf{u}\cdot\nabla\phi_{\mathrm{n}} = D_{\mathrm{n}}\Delta\phi_{\mathrm{n}} - R(c)\phi_{\mathrm{n}} \tag{2.4}$$

$$\frac{\partial\phi_{\mathrm{a}}}{\partial t} + \mathbf{u}\cdot\nabla\phi_{\mathrm{a}} = R(c)\phi_{\mathrm{n}} \tag{2.5}$$

$$c_t + \mathbf{u} \cdot \nabla c = D_c \Delta c + AR(c)\phi_n - Kc \tag{2.6}$$

$$E_t + \mathbf{u} \cdot \nabla_x E + (\mathbf{y} \cdot \nabla \mathbf{u}) \cdot \nabla_y E = \alpha(|\mathbf{y}|)\phi_a{}^2 - \beta(|\mathbf{y}|)E \tag{2.7}$$

$$\mathbf{f}^p = 1/2 \int \mathbf{y} \cdot \nabla_x E(\mathbf{x}, \mathbf{y}, t)\ S(|\mathbf{y}|)\mathbf{y}\, d\mathbf{y} \tag{2.8}$$

Equations (2.2)–(2.3) are the Navier–Stokes equations which describe the dynamics of a viscous incompressible fluid (Batchelor, 1967) of constant density ρ and constant viscosity μ. The force density term $\mathbf{f}$ in (2.2) arises, in part, from cohesive bonds between activated platelets. That is, one of the contributions to $\mathbf{f}$ comes from the term $\mathbf{f}^p$ defined in (2.8). Equation (2.4) expresses the assumption that non-activated platelets are transported by advection with velocity $\mathbf{u}$ and diffusion with diffusion coefficient D_n, and are converted to activated platelets at a rate $R(c)\phi_n$ which depends on the concentration c of activating chemical. Equation (2.5) describes the transport of activated platelets by advection and their creation by the activation of non-activated platelets. Diffusive transport of platelets is included in the model to reflect the experimental observation that in flowing blood platelets have a random component to their motion two orders of magnitude larger than that which would result from Brownian motion (Turitto *et al.*, 1972). The enhanced diffusivity is correlated with the presence of the larger and more numerous red blood cells which make up 45% of the volume of normal blood (Goldsmith & Karino, 1977; Wang & Keller, 1985). It is thought that shear-induced tumbling and colliding of the non-spherical red blood cells causes a local mixing of the blood, thus imparting to the platelets a diffusion-like motion (Turitto & Baumgartner, 1975; Wang & Keller, 1985). We expect that the influence of these local disturbances on a particle's motion decreases as the size of the particle increases, and that the influence of these disturbances is small for all particles in a region where the density of aggregates is high. Thus, the diffusivity of individual non-activated platelets should be greater than that of aggregated activated platelets, and both diffusivities should decrease with increasing aggregate density. For simplicity, we have assumed that non-activated platelets have a positive constant diffusivity while activated platelets have zero diffusivity. Equation (2.6) states that the activating chemical is transported by advection and diffusion, is created when non-activated platelets are activated, and is degraded in time. The rate of creation is the amount A of activating chemical that a single platelet secretes upon activation multiplied by the rate $R(c)\phi_n$ at which non-activated platelets are activated.

The derivations of (2.7) and (2.8) are reviewed in Appendices A and B because very similar derivations lead to the new equations which describe platelet–wall adhesion. Equation (2.7) describes the transport of platelet–platelet elastic bonds by advection in $\mathbf{x}$-space at velocity $\mathbf{u}$ and by advection in $\mathbf{y}$-space at velocity $\mathbf{y} \cdot \nabla \mathbf{u}$. This last term originates in the small difference between the velocity $\mathbf{u}$ at the two ends of a platelet–platelet bond ($\mathbf{x}$ and $\mathbf{x} + \epsilon\mathbf{y}$). Equation (2.7) also reflects the creation of new interplatelet bonds between activated platelets at a rate $\alpha(|\mathbf{y}|)$ per pair of activated platelets, and the breaking of existing interplatelet bonds at a rate $\beta(|\mathbf{y}|)$. Because only nearby platelets can cohere, the link-creation rate function $\alpha(|\mathbf{y}|)$ is assumed to drop rapidly to 0 when $|\mathbf{y}|$ grows much larger than 1. The link-breaking function $\beta(|\mathbf{y}|)$ in general should increase sharply with $|\mathbf{y}| > 1$ to reflect faster breaking of links under strain. As we discuss below, incorporating strain-dependent breaking into the model poses substantial challenges, and so in Fogelson (1992, 1993) only the case $\beta(|\mathbf{y}|) = \beta_0$ constant was considered.

Equation (2.8) gives the force density on the fluid generated by interplatelet bonds and is derived in Appendix B. The integral in (2.8) is over all of **y**-space, but because $E(\mathbf{x}, \mathbf{y}, t)$ decays rapidly for $|\mathbf{y}| \gg 1$, the domain of integration is effectively finite. The cohesion force density $\mathbf{f}^{\mathrm{p}}$ can also be obtained as the divergence of the cohesion stress tensor $\underline{\underline{\sigma}}^{\mathrm{p}}(\mathbf{x}, t)$ defined by

$$\underline{\underline{\sigma}}^{\mathrm{p}}(\mathbf{x}, t) = \frac{1}{2} \int E(\mathbf{x}, \mathbf{y}, t) S(|\mathbf{y}|) \mathbf{y}\mathbf{y}^T \, \mathrm{d}\mathbf{y}. \tag{2.9}$$

As was shown in Fogelson (1992), under the assumptions that each interplatelet link behaves as a linear spring with zero resting length ($S(|\mathbf{y}|) = K_0$) and that the rate at which links break $\beta(|\mathbf{y}|)$ is a constant β_0, then the model equations can be used to derive the following partial differential equation for the cohesion-stress tensor $\underline{\underline{\sigma}}^{\mathrm{p}}$:

$$\underline{\underline{\sigma}}^{\mathrm{p}}_t + \mathbf{u} \cdot \nabla \underline{\underline{\sigma}}^{\mathrm{p}} = \underline{\underline{\sigma}}^{\mathrm{p}} \underline{\underline{\nabla \mathbf{u}}} + (\underline{\underline{\sigma}}^{\mathrm{p}} \underline{\underline{\nabla \mathbf{u}}})^T + a_2 {\phi_{\mathrm{a}}}^2 \underline{\underline{I}} - \beta_0 \underline{\underline{\sigma}}^{\mathrm{p}}. \tag{2.10}$$

Here, a_2 is a constant proportional to the second moment of $\alpha(|\mathbf{y}|)S(|\mathbf{y}|)$, $\underline{\underline{I}}$ is the identity tensor, and the tensor $\underline{\underline{\nabla \mathbf{u}}}$ has ijth element $\frac{\partial u_j}{\partial x_i}$. In (2.10) all reference to the link vectors **y** disappears. Since $\underline{\underline{\sigma}}^{\mathrm{p}}$ is a symmetric tensor, the above tensor equation amounts to solving three equations (in the two-dimensional case). Once we have $\underline{\underline{\sigma}}^{\mathrm{p}}$, $\mathbf{f}^{\mathrm{p}}$ is obtained by differentiation from the equation

$$\mathbf{f}^{\mathrm{p}} = \nabla \cdot \underline{\underline{\sigma}}^{\mathrm{p}}. \tag{2.11}$$

Because (2.10) involves half as many spatial variables as (2.7), computing the solution to (2.10) and then using (2.11) to obtain $\mathbf{f}^{\mathrm{p}}$ is a much more efficient process than is computing E from (2.7) and then integrating over **y**-space to obtain $\mathbf{f}^{\mathrm{p}}$. It is important to notice that in this model, the formation of an aggregate does *not* change the domain in which the Navier–Stokes equations are solved. The fluid dynamics equations hold everywhere, and the formation of an aggregate manifests itself on the fluid motion solely through the force density term $\mathbf{f}^{\mathrm{p}}$. For later reference, we note that if $\beta(|\mathbf{y}|) = \beta_0$, then z^{p} satisfies the equation

$$z^{\mathrm{p}}_t + \mathbf{u} \cdot \nabla z^{\mathrm{p}} = a_0 {\phi_{\mathrm{a}}}^2 - \beta_0 z^{\mathrm{p}}, \tag{2.12}$$

where a_0 is the integral of $\alpha(|\mathbf{y}|)$.

Among the results presented in Fogelson (1992, 1993) are numerical studies of the development of an aggregate in a background flow. Because of the absence of platelet–wall interactions in those papers, we used a background stagnation point flow and relied on symmetry to fix in place the centre of the developing aggregate. A typical numerical experiment began with a uniform concentration of non-activated platelets ϕ_{n}, no activated platelets ϕ_{a}, and therefore no interplatelet elastic links. At $t = 0$, activating chemical at a concentration c sufficient to cause activation was added in a small circular region centred on the stagnation point. As a consequence, platelet activation began, more activating chemical was released, and activated platelets began to form interplatelet links. The links formed isotropically (see the link formation terms in (2.7) and (2.10)) but the link distribution was subsequently skewed as the stagnation point flow elongated the initially

circular aggregate into an ellipse of increasing eccentricity. With further time, the size of the aggregate grew because of advective and diffusive transport of the activating chemical and consequent platelet activation and link formation, and the links continued to skew to align increasingly with the flow. Eventually the interplatelet links generated enough force on the fluid to bring the fluid velocity within the aggregate to zero, and the shape and size of the aggregate stabilized. In effect, the composite fluid-, platelet-, elastic link material which comprises an aggregate in these models had undergone a chemically-induced phase transition from the state of behaving as a viscous fluid, to a state of behaving as a visco-elastic solid. More information about these and other results from the solution-phase aggregation models can be found in Fogelson (1992, 1993) and Wang & Fogelson (1999).

3. Strain-dependent link breaking

Through the elastic link distribution function, $E(\mathbf{x}, \mathbf{y}, t)$, the general form of the model describes both macro- and micro-scale events. Using the evolution equation (2.7) for E, multiplying it by $1/2\, S(|\mathbf{y}|)\mathbf{y}\mathbf{y}^T$, and integrating with respect to $\mathbf{y}$, we can derive the following equation for the cohesion stress tensor $\underline{\underline{\sigma}}^{\mathrm{p}}$:

$$\underline{\underline{\sigma}}^{\mathrm{p}}_t + \mathbf{u} \cdot \nabla \underline{\underline{\sigma}}^{\mathrm{p}} = \underline{\underline{\sigma}}^{\mathrm{p}} \underline{\underline{\nabla \mathbf{u}}} + (\underline{\underline{\sigma}}^{\mathrm{p}} \underline{\underline{\nabla \mathbf{u}}})^T + a_2\, \phi_a^2\, \underline{\underline{I}} + 1/2 \int (\mathbf{y}^T \underline{\underline{\nabla \mathbf{u}}}\, \mathbf{y}) \frac{S'(|\mathbf{y}|)}{|\mathbf{y}|}\, E\, \mathbf{y}\mathbf{y}^T \, \mathrm{d}\mathbf{y}$$
$$-1/2 \int \beta(|\mathbf{y}|)\, E\, S(|\mathbf{y}|)\mathbf{y}\mathbf{y}^T \, \mathrm{d}\mathbf{y}. \tag{3.1}$$

For the remainder of the paper we assume that the links behave like linear springs, so that $S'(|\mathbf{y}|) = 0$ and the fourth term on the right side vanishes. For a breaking rate $\beta(|\mathbf{y}|) = \beta_0$ which is independent of the link length $|\mathbf{y}|$, the last term on the right side simplifies to $\beta_0 \underline{\underline{\sigma}}^{\mathrm{p}}$, and we obtain the special form of the model considered above. In order to study breakup (embolization) of an aggregate as well as the possibility that shear stresses limit the growth of an aggregate, we want to be able to treat the more general case in which the breaking rate does depend on how strained the aggregate is locally. One way to do this is to solve the general form of the model including (2.7) and (2.8). In Wang & Fogelson (1999), we describe a computational method for doing this as well as some examples of how a strain-dependent breaking rate leads to different behaviour than a constant breaking rate. These calculations are expensive. Even though we limit ourselves to the two-dimensional case, because of the presence of two sets of spatial variables, (2.7) involves four spatial variables as well as time. An alternative, adapted from ideas in the polymer literature (Phan-Thien & Tanner, 1977), is to allow the breaking rate to vary, but as a function only of macroscale quantities. In this case, the function β can be pulled out of the integral in the last term in (3.1) and this term reduces to the breaking rate times $\underline{\underline{\sigma}}^{\mathrm{p}}$. In the rest of this paper, we assume that β is a function of the ratio of the trace of the stress tensor $\mathrm{Tr}(\underline{\underline{\sigma}}^{\mathrm{p}})$ and the total link density z^{p} at $\mathbf{x}$. That is, we assume

$$\beta = \beta\left(\frac{\mathrm{Tr}(\underline{\underline{\sigma}}^{\mathrm{p}})}{z^{\mathrm{p}}}\right). \tag{3.2}$$

There are two interpretations of $\mathrm{Tr}(\underline{\underline{\sigma}}^{\mathrm{p}})/z^{\mathrm{p}}$ that make this a reasonable assumption. From the definitions of $\underline{\underline{\sigma}}^{\mathrm{p}}$ and z^{p}, we see that

$$\frac{\mathrm{Tr}(\underline{\underline{\sigma}}^{\mathrm{p}})}{z^{\mathrm{p}}} = \frac{\int 1/2\, S_0\, |\mathbf{y}|^2\, E(\mathbf{x}, \mathbf{y}, t)\, \mathrm{d}\mathbf{y}}{z^{\mathrm{p}}} = \frac{S_0}{2} \left\{ \frac{\int E(\mathbf{x}, \mathbf{y}, t)\, |\mathbf{y}|^2\, \mathrm{d}\mathbf{y}}{\int E(\mathbf{x}, \mathbf{y}, t)\, \mathrm{d}\mathbf{y}} \right\}. \tag{3.3}$$

The integral which defines $\mathrm{Tr}(\underline{\underline{\sigma}}^{\mathrm{p}})$ in the middle expression is the total elastic strain energy per unit volume due to links emanating from activated platelets at $\mathbf{x}$, so the middle expression has the interpretation of being the average strain energy per link. The expression on the right shows that $\mathrm{Tr}(\underline{\underline{\sigma}}^{\mathrm{p}})/z^{\mathrm{p}}$ is proportional to the mean-squared link length and so it is a useful surrogate argument for a length-dependent function. With the new assumption about the nature of the function β, the equation for $\underline{\underline{\sigma}}^{\mathrm{p}}$ is

$$\underline{\underline{\sigma}}^{\mathrm{p}}_t + \mathbf{u} \cdot \nabla \underline{\underline{\sigma}}^{\mathrm{p}} = \underline{\underline{\sigma}}^{\mathrm{p}} \underline{\underline{\nabla \mathbf{u}}} + (\underline{\underline{\sigma}}^{\mathrm{p}} \underline{\underline{\nabla \mathbf{u}}})^T + a_2 {\phi_{\mathrm{a}}}^2 \underline{\underline{I}} - \beta \left(\frac{\mathrm{Tr}(\underline{\underline{\sigma}}^{\mathrm{p}})}{z^{\mathrm{p}}} \right) \underline{\underline{\sigma}}^{\mathrm{p}}, \tag{3.4}$$

and the equation for z^{p} is

$$z^{\mathrm{p}}_t + \mathbf{u} \cdot \nabla z^{\mathrm{p}} = a_0 {\phi_{\mathrm{a}}}^2 - \beta \left(\frac{\mathrm{Tr}(\underline{\underline{\sigma}}^{\mathrm{p}})}{z^{\mathrm{p}}} \right) z^{\mathrm{p}}. \tag{3.5}$$

See Guy (2004) for an analysis of the asymptotic behaviour of the model with this form of β as well as a comparison with the behaviour of the full model for shear flow. There it is shown that defining β to be a function of averaged quantities in this way accurately captures the behaviour of the full model ($\beta = \beta(|\mathbf{y}|)$) for steady shear flows at all shear rates. It is convenient to denote by $\mathcal{E}$ the average strain energy per link $\mathrm{Tr}(\underline{\underline{\sigma}}^{\mathrm{p}})/z^{\mathrm{p}}$. Then, the breaking rate function we use in the current paper is

$$\beta(\mathcal{E}) = \begin{cases} \beta_0, & \text{for } \mathcal{E} \leqslant \mathcal{E}_0 \\ \beta_0 \exp(\beta_1(\mathcal{E} - \mathcal{E}_0)) & \text{for } \mathcal{E} > \mathcal{E}_0 \end{cases} \tag{3.6}$$

where β_1 is a positive constant and $\mathcal{E}_0 = (3a_2)/a_0$. From (3.4) and (3.5), we see that $\mathcal{E}_0$ can be interpreted as the average energy at which links form, and so we are assuming that links break at an accelerated rate only when the average strain energy per link is greater than the average strain energy per link at which links form.

4. Platelet–surface interactions

There are two major aspects to platelet interactions with the vessel wall: one is biochemical and involves activation of platelets which contact appropriate proteins embedded in the vessel wall. The second is mechanical and involves the adhesion of platelets to the wall. Below we describe how each of these interactions is incorporated in a natural way into the models described above. First we discuss how we model the walls themselves as well as other surfaces that may contact the blood. Our goal is to be able to deal with vessels of complex shape (e.g. a bifurcating vessel, or a vessel partially occluded by an atherosclerotic plaque), as well as other objects immersed in the blood, such as prosthetic cardiac valves, which influence the flow, and with which platelets might react.

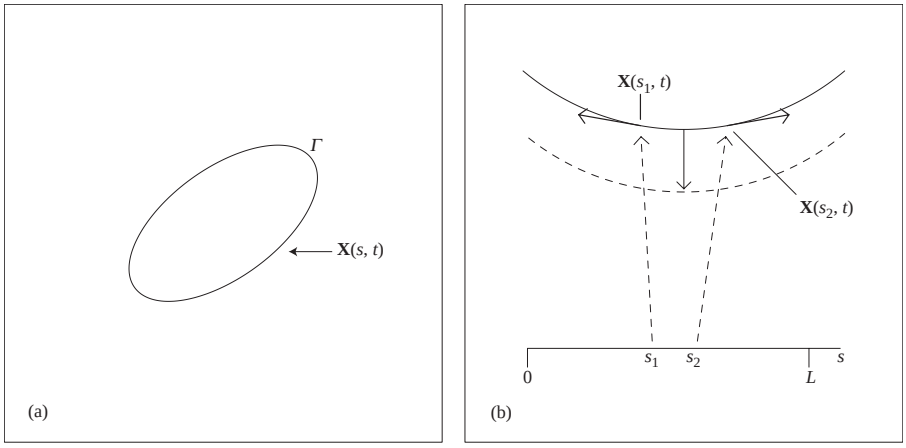

FIG. 2. Immersed boundary schematic. (a) Example immersed boundary curve Γ described by function $\mathbf{X}(s, t)$. (b) Small sections of an immersed boundary curve (solid) and target 'tether-point' curve (dashed). The section of the immersed boundary surface between the points $\mathbf{X}(s_1, t)$ and $\mathbf{X}(s_2, t)$ is subject to forces (solid arrows) (i) intended to keep it at the target location and (ii) because of tension in the immersed boundary itself arising from its deformation or stretching.

4.1 *Modelling of blood-contacting surfaces*

Our approach to modelling the vessel walls is based on the immersed boundary method originally introduced by Peskin for modelling blood flow in the heart. Since this method has been described extensively elsewhere (e.g. Fauci & Fogelson, 1993; Peskin, 1977; Peskin & McQueen, 1980, 1993) we will only sketch the method and explain how we use it for the present studies.

The immersed boundary method solves the coupled equations of motion of a viscous, incompressible fluid and one or more massless elastic surfaces or objects immersed in the fluid. An Eulerian description based on the Navier–Stokes equations is used for the fluid dynamics and a Lagrangian description is used for each object immersed in the fluid. For example, suppose we have a single immersed boundary curve Γ as shown in Fig. 2(a). The locations of points on Γ are given by the vector function $\mathbf{X}(s, t)$. Here, the parameter s indicates arclength along Γ in some reference configuration. As s varies between 0 and L, $\mathbf{X}(s, t)$ sweeps through the points on the immersed boundary curve. Each value of s refers to a particular material point on the immersed boundary, and the function $\mathbf{X}(s, t)$ with s held fixed describes the trajectory of this point in time. Each immersed boundary point is in contact with the surrounding fluid, and so its velocity must be consistent with the no-slip boundary condition. This gives us the equation of motion for the point as

$$\frac{\partial \mathbf{X}(s, t)}{\partial t} = \mathbf{u}(\mathbf{X}(s, t), t) = \int \mathbf{u}(\mathbf{x}, t)\delta(\mathbf{x} - \mathbf{X}(s, t))\, \mathrm{d}\mathbf{x}, \tag{4.1}$$

where δ represents the two-dimensional Dirac delta function.

Deformation of the immersed boundary curve from a prescribed equilibrium shape and size, or displacement of the immersed boundary curve from a prescribed equilibrium location, can lead to the generation of forces at each point $\mathbf{X}(s, t)$ on

the immersed boundary. These forces are described by a (prescribed) force density function $\mathbf{F}(\mathbf{X}(\cdot, t), s, t)$ which has units of force per unit s. The values of $\mathbf{F}(\mathbf{X}(\cdot, t), s, t)$ are determined by the current configuration of the immersed boundary points. More specifically, we assume that the tension force in the boundary curve at point $\mathbf{X}(s, t)$ is

$$T\left(\left|\frac{\partial \mathbf{X}}{\partial s}\right|, s, t\right)\mathbf{t} \tag{4.2}$$

where

$$\mathbf{t} = \frac{\partial \mathbf{X}}{\partial s} \Big/ \left|\frac{\partial \mathbf{X}}{\partial s}\right| \tag{4.3}$$

is the unit tangent to the immersed boundary curve. That is, we assume that the tension is a function of the local stretching of Γ as indicated by $\left|\frac{\partial \mathbf{X}}{\partial s}\right|$. It follows that the force density (per unit s) along the curve is

$$\frac{\partial}{\partial s}(T\mathbf{t}) = \frac{\partial T}{\partial s}\mathbf{t} + T\frac{\partial \mathbf{t}}{\partial s}, \tag{4.4}$$

which can have components in directions tangential and normal to Γ. In addition, we assume that there is a force which acts to 'tether' each point $\mathbf{X}(s, t)$ on Γ to a corresponding point $\mathbf{X}^{\text{teth}}(s)$ on a target (or tether) equilibrium curve. The force density associated with this is given by the expression

$$-S\left(\mathbf{X}(s, t) - \mathbf{X}^{\text{teth}}(s)\right) \tag{4.5}$$

where the stiffness parameter S has units of force per unit area. These contributions to the force density $\mathbf{F}$ are depicted in Fig. 2(b). A third type of immersed boundary force $\mathbf{F}_{\text{cl}}$ (cl stands for cross-link) is used in the simulations below to make the walls more rigid. It arises from elastic links between points on two distinct but approximately parallel boundary curves. This is described in Section 5. Taking the three types of contributions into account, $\mathbf{F}$ is given by

$$\mathbf{F}(\mathbf{X}(\cdot, t), s, t) = \frac{\partial}{\partial s}(T\mathbf{t}) \; - \; S\left(\mathbf{X}(s, t) - \mathbf{X}^{\text{teth}}(s)\right) + \mathbf{F}_{\text{cl}}. \tag{4.6}$$

These immersed boundary forces act on the surrounding fluid. In fact, because the immersed boundary itself is assumed to have no mass, these forces are transmitted completely to the fluid. This transmission is accomplished by integrating $\mathbf{F}(\mathbf{X}(\cdot, t), s, t)\ \delta(\mathbf{x} - \mathbf{X}(s, t))$ over the immersed boundary. If there are N immersed boundaries, then each contributes to the total force density driving the fluid motion. The total force density due to the immersed boundaries is then

$$\mathbf{f}^{\text{ib}}(\mathbf{x}, t) = \sum_{i=1}^{N} \int_0^{L_i} \mathbf{F}(\mathbf{X}_i(\cdot, t), s, t)\delta(\mathbf{x} - \mathbf{X}_i(s, t))\, \mathrm{d}s. \tag{4.7}$$

Since each integral here is over a one-dimensional immersed boundary and involves a two-dimensional delta-function, the resulting force density $\mathbf{f}^{\text{ib}}$ is concentrated in thin layers

along each immersed boundary. In a pure immersed boundary calculation, this would be the force density which appears in the Navier–Stokes equations, equation (2.2). In the context of this paper, $\mathbf{f}^{\mathrm{ib}}$ is one of several contributors to $\mathbf{f}$ in (2.2). For actual immersed boundary simulations, the model system given by (2.2), (2.3), (4.1)–(4.7) is approximated by a discrete system of algebraic equations which is described in Section 5.

4.2 *Equations describing platelet–wall interactions*

To describe these interactions, we begin by defining the density of reactive wall sites $W(\mathbf{X}(t), t)$ at a point $\mathbf{X}(t)$ on the vessel wall. W will be positive only on injured portions of the wall. This surface density is converted to a volume concentration using a formula analogous to that in (4.7) for the immersed boundary force density $\mathbf{f}^{\mathrm{ib}}$:

$$w(\mathbf{x}, t) = \sum_{i=1}^{N} \int_0^{L_i} W(\mathbf{X}_i(\cdot, t), s, t)\delta(\mathbf{x} - \mathbf{X}_i(s, t))\, \mathrm{d}s. \tag{4.8}$$

The function w is the volume concentration of reactive sites on the walls, and is non-zero only in thin layers along prescribed portions of the blood-contacting surfaces. While it might seem more natural to define a surface density of reactive sites only on the walls, we find that defining a non-zero volume concentration in thin layers near the walls facilitates deriving model equations and implementing their numerical solution. Also, this approach is consistent in philosophy with the immersed boundary method's treatment of the walls as thin layers of force density applied to the fluid. We note that $w(\mathbf{x}, t)$ is defined in reference to blood-contacting surfaces, which in turn are represented by immersed boundaries as described above. Because immersed boundary points move at the local fluid velocity (see (4.1)), w is also advected with the flow. That is, w satisfies the equation

$$w_t + \mathbf{u} \cdot \nabla w = 0,$$

provided, as assumed in this paper, that W does not depend explicitly on t. It is not necessary to solve this equation to determine w because we track the positions of the immersed boundary points with reference to which w is defined. Note that for surfaces that are tethered strongly, there is little motion, and so any non-zero values of w associated with such surfaces are effectively fixed in space.

Because of the dual mechanical and biochemical nature of platelets' interactions with the walls, it would be reasonable to define *two* populations of reactive wall sites, one for each type of interaction. For biological surfaces (e.g. blood vessel walls), both interactions involve the same surface-bound proteins so it is reasonable to describe both types of interactions in terms of a single population of reactive wall sites. For artificial surfaces such as prosthetic cardiac valves, different components of the surface may trigger the different responses, and so two (or more) populations of reactive sites would be useful. In the equations below, we assume that there is one population of reactive sites responsible for both biochemical and mechanical interactions, but it should be clear how to modify our equations to incorporate separate populations of reactive sites.

To reflect platelet activation by contact with injured vessel walls or artificial surfaces,

we modify the transport equations (2.4)–(2.6) for ϕ_n, ϕ_a, and c to be

$$(\phi_n)_t + \mathbf{u}\cdot\nabla\phi_n = D_n\Delta\phi_n - \big(R(c) + R^w(w)\big)\phi_n \tag{4.9}$$

$$(\phi_a)_t + \mathbf{u}\cdot\nabla\phi_a = \big(R(c) + R^w(w)\big)\phi_n \tag{4.10}$$

$$c_t + \mathbf{u}\cdot\nabla c = D_c\Delta c + A\big(R(c) + R^w(w)\big)\phi_n. \tag{4.11}$$

The new term in (4.9) and (4.10) is $R^w(w)\phi_n$ which is the rate of activation of non-activated platelets of concentration ϕ_n when in contact with reactive wall sites at concentration w. This term enters in (4.9) with a minus sign to reflect a decrease in ϕ_n due to activation, and in (4.10) with a plus sign to reflect a corresponding increase in ϕ_a. The rate functions $R^w(w)$ is 0 when $w = 0$ so the new terms are concentrated only in thin layers near portions of the bounding surfaces. The new term in (4.11), $AR^w(w)\phi_n$, is the rate of release of activating chemical because of activation of platelets caused by their contact with the walls.

To include in the model adhesion between activated platelets and reactive ('sticky') wall sites, we define $\widetilde{E}^w(\mathbf{x}, \mathbf{r}, t)$ so that $\widetilde{E}^w(\mathbf{x}, \mathbf{r}, t)d\mathbf{r}$ is the concentration of (adhesive) links which connect activated platelets at $\mathbf{x}$ to wall sites at $\mathbf{x}+\mathbf{r}$. We again change variables by letting $\mathbf{r} = \epsilon\mathbf{y}$ and $E^w(\mathbf{x}, \mathbf{y}, t) = \epsilon^3\widetilde{E}^w(\mathbf{x}, \mathbf{r}, t)$. Then $E^w(\mathbf{x}, \mathbf{y}, t)$ satisfies the equation

$$E^w_t + \mathbf{u}\cdot\nabla_x E^w + (\mathbf{y}\cdot\nabla\mathbf{u})\cdot\nabla_y E^w = \alpha^w(|\mathbf{y}|)\phi_a\, w - \beta^w(|\mathbf{y}|)E^w. \tag{4.12}$$

This is very similar to the transport equation (2.10) satisfied by the interplatelet link density $E(\mathbf{x}, \mathbf{y}, t)$ except that the term $\alpha(|\mathbf{y}|)\phi_a{}^2$ from (2.10) is here replaced by the term $\alpha^w(|\mathbf{y}|)\phi_a\, w$. The change reflects the fact that the links described by E^w connect elements of distinct species, platelets and reactive wall sites. We refer to $\alpha^w(|\mathbf{y}|)$ and $\beta^w(|\mathbf{y}|)$ as the adhesive-link formation and breaking rates, respectively. The function $\alpha^w(|\mathbf{y}|)$ decays quickly for $|\mathbf{y}| > 1$, and the function $\beta^w(|\mathbf{y}|)$ ideally increases sharply for $|\mathbf{y}| > 1$ because of strain-induced breaking of the platelet–wall links.

Just as the stress tensor $\underline{\underline{\sigma}}^p$ is associated with the cohesive force density $\mathbf{f}^p$, a stress tensor $\underline{\underline{\sigma}}^w$ is associated with the adhesive force density $\mathbf{f}^w$. The adhesive stress tensor is defined by

$$\underline{\underline{\sigma}}^w(\mathbf{x}, t) = \frac{1}{2}\int E^w(\mathbf{x}, \mathbf{y}, t)S^w(|\mathbf{y}|)\mathbf{y}\mathbf{y}^T\, d\mathbf{y}. \tag{4.13}$$

To allow the adhesive links to break in a strain-dependent way without having to explicitly deal with the microscopic scale, we assume that

$$\beta^w = \beta^w\left(\frac{\mathrm{Tr}(\underline{\underline{\sigma}}^w)}{z^w}\right). \tag{4.14}$$

where $z^w(\mathbf{x}, t) = \int E^w(\mathbf{x}, \mathbf{y}, t)d\mathbf{y}$. With this assumption, $\underline{\underline{\sigma}}^w$ satisfies the equation

$$\underline{\underline{\sigma}}^w_t + \mathbf{u}\cdot\nabla\underline{\underline{\sigma}}^w = \underline{\underline{\sigma}}^w\underline{\underline{\nabla\mathbf{u}}} + (\underline{\underline{\sigma}}^w\underline{\underline{\nabla\mathbf{u}}})^T + a_2^w\phi_a\, w\underline{\underline{I}} - \beta^w\left(\frac{\mathrm{Tr}(\underline{\underline{\sigma}}^w)}{z^w}\right)\underline{\underline{\sigma}}^w, \tag{4.15}$$

and the concentration of platelet–wall links z^w satisfies

$$z^w_t + \mathbf{u}\cdot\nabla z^w = a_0^w\phi_a w - \beta^w\left(\frac{\mathrm{Tr}(\underline{\underline{\sigma}}^w)}{z^w}\right)z^w. \tag{4.16}$$

Once $\underline{\underline{\sigma}}^{\mathrm{w}}$ is known, the adhesive force density may be calculated from

$$\mathbf{f}^{\mathrm{w}}(\mathbf{x}, t) = \nabla \cdot \underline{\underline{\sigma}}^{\mathrm{w}}(\mathbf{x}, t). \tag{4.17}$$

The final element of the platelet–wall interaction is specification of boundary conditions at the wall for the diffusing species ϕ_{n} and c. Platelets certainly do not cross the vessel wall, and we are aware of no evidence that the signalling chemical permeates the wall. Therefore for both ϕ_{n} and c, we impose no flux boundary conditions along the immersed boundaries.

4.3 *Fluid force density*

We have described three different types of forces which each contribute to the force density $\mathbf{f}$ which drives the fluid motion. The first is $\mathbf{f}^{\mathrm{ib}}$, the force density generated by the immersed boundaries and which represents the mechanical properties of the blood-contacting surfaces. The second is $\mathbf{f}^{\mathrm{p}}$, the cohesive-force density which arises from links between pairs of activated platelets. The third is $\mathbf{f}^{\mathrm{w}}$, the adhesive-force density which is generated by links between activated platelets and sticky sites on the surfaces in contact with the blood. It is also sometimes useful to specify an exogenous force density $\mathbf{f}^{\mathrm{g}}$ to drive a background flow. For example, a uniform $\mathbf{f}^{\mathrm{g}}$ corresponds to a spatially constant pressure gradient (see Section 5.6 for details). Taking all of these into account, the force density in the Navier–Stokes equations becomes

$$\mathbf{f}(\mathbf{x}, t) = \mathbf{f}^{\mathrm{g}} + \mathbf{f}^{\mathrm{p}} + \mathbf{f}^{\mathrm{w}} + \mathbf{f}^{\mathrm{ib}}.$$

4.4 *Model summary*

For the remainder of this paper we will focus on the form of the aggregation models in which evolution equations (3.4), (4.15) for the cohesion stress tensor $\underline{\underline{\sigma}}^{\mathrm{p}}$ and the adhesion stress tensor $\underline{\underline{\sigma}}^{\mathrm{w}}$ are solved, and the cohesion and adhesion force densities are obtained by calculating the divergence of these respective tensors. For convenience, we summarize the equations of this form of the model here:

$$\rho(\mathbf{u}_t + \mathbf{u} \cdot \nabla \mathbf{u}) = -\nabla p + \mu \Delta \mathbf{u} + \mathbf{f} \tag{4.18}$$

$$\nabla \cdot \mathbf{u} = 0 \tag{4.19}$$

$$(\phi_{\mathrm{n}})_t + \mathbf{u} \cdot \nabla \phi_{\mathrm{n}} = D_{\mathrm{n}} \Delta \phi_{\mathrm{n}} - \big(R(c) + R^{\mathrm{w}}(w)\big)\phi_{\mathrm{n}} \tag{4.20}$$

$$(\phi_{\mathrm{a}})_t + \mathbf{u} \cdot \nabla \phi_{\mathrm{a}} = \big(R(c) + R^{\mathrm{w}}(w)\big)\phi_{\mathrm{n}} \tag{4.21}$$

$$c_t + \mathbf{u} \cdot \nabla c = D_{\mathrm{c}} \Delta c + A\big(R(c) + R^{\mathrm{w}}(w)\big)\phi_{\mathrm{n}} - Kc \tag{4.22}$$

$$\underline{\underline{\sigma}}^{\mathrm{p}}_t + \mathbf{u} \cdot \nabla \underline{\underline{\sigma}}^{\mathrm{p}} = \underline{\underline{\sigma}}^{\mathrm{p}} \underline{\underline{\nabla \mathbf{u}}} + (\underline{\underline{\sigma}}^{\mathrm{p}} \underline{\underline{\nabla \mathbf{u}}})^T + a_2 {\phi_{\mathrm{a}}}^2 \underline{\underline{I}} - \beta \left(\frac{\mathrm{Tr}(\underline{\underline{\sigma}}^{\mathrm{p}})}{z^{\mathrm{p}}} \right) \underline{\underline{\sigma}}^{\mathrm{p}} \tag{4.23}$$

$$\mathbf{f}^{\mathrm{p}}(\mathbf{x}, t) = \nabla \cdot \underline{\underline{\sigma}}^{\mathrm{p}}(\mathbf{x}, t) \tag{4.24}$$

$$z^{\mathrm{p}}_t + \mathbf{u} \cdot \nabla z^{\mathrm{p}} = a_0 {\phi_{\mathrm{a}}}^2 - \beta \left(\frac{\mathrm{Tr}(\underline{\underline{\sigma}}^{\mathrm{p}})}{z^{\mathrm{p}}} \right) z^{\mathrm{p}}. \tag{4.25}$$

$$\underline{\underline{\sigma}}^{\mathrm{w}}_t + \mathbf{u} \cdot \nabla \underline{\underline{\sigma}}^{\mathrm{w}} = \underline{\underline{\sigma}}^{\mathrm{w}} \underline{\underline{\nabla \mathbf{u}}} + (\underline{\underline{\sigma}}^{\mathrm{w}} \underline{\underline{\nabla \mathbf{u}}})^T + a_2^{\mathrm{w}} \phi_{\mathrm{a}} w \underline{\underline{I}} - \beta^{\mathrm{w}} \left(\frac{\mathrm{Tr}(\underline{\underline{\sigma}}^{\mathrm{w}})}{z^{\mathrm{w}}} \right) \underline{\underline{\sigma}}^{\mathrm{w}} \tag{4.26}$$

$$\mathbf{f}^{\mathrm{w}}(\mathbf{x},t) = \nabla \cdot \underline{\underline{\sigma}}^{\mathrm{w}}(\mathbf{x},t) \tag{4.27}$$

$$z_t^{\mathrm{w}} + \mathbf{u}\cdot\nabla z^{\mathrm{w}} = a_0^{\mathrm{w}}\phi_{\mathrm{a}} w - \beta^{\mathrm{w}}\left(\frac{\mathrm{Tr}(\underline{\underline{\sigma}}^{\mathrm{w}})}{z^{\mathrm{w}}}\right) z^{\mathrm{w}} \tag{4.28}$$

$$\frac{\partial \mathbf{X}(s,t)}{\partial t} = \mathbf{u}(\mathbf{X}(s,t),t) = \int \mathbf{u}(\mathbf{x},t)\delta(\mathbf{x}-\mathbf{X}(s,t))\mathrm{d}\mathbf{x} \tag{4.29}$$

$$\mathbf{F}(\mathbf{X}(\cdot,t),s,t) = \frac{\partial}{\partial s}(T\mathbf{t}) \; - \; S\left(\mathbf{X}(s,t) - \mathbf{X}^{\mathrm{teth}}(s)\right) + \mathbf{F}_{\mathrm{cl}} \tag{4.30}$$

$$\mathbf{f}^{\mathrm{ib}}(\mathbf{x},t) = \sum_{i=1}^{N}\int_0^{L_i} \mathbf{F}(\mathbf{X}_i(\cdot,t),s,t)\delta(\mathbf{x}-\mathbf{X}_i(s,t))\,\mathrm{d}s \tag{4.31}$$

$$\mathbf{f}(\mathbf{x},t) = \mathbf{f}^{\mathrm{g}} + \mathbf{f}^{\mathrm{p}} + \mathbf{f}^{\mathrm{w}} + \mathbf{f}^{\mathrm{ib}}. \tag{4.32}$$

5. Computational methods for the aggregation model

The computational solution of the aggregation models presents several challenges: (1) the models involve a large number of coupled nonlinear partial differential equations; (2) the models involve a mix of Eulerian and Lagrangian descriptions and communicating between these is required; (3) the combination of rapid localized reactions and small diffusion coefficients leads to the presence of steep spatial gradients; (4) transport of platelets and chemicals needs to be confined to the portions of the domain inside of the immersed boundaries used to represent the vessel walls; (5) the fluid–wall and fluid–platelet interactions can be stiff and present difficulties in achieving stable calculations. In this section, we describe the numerical methods we have assembled to meet these challenges.

We solve the model equations in a rectangular region $R = [0, x_{\max}] \times [0, y_{\max}]$. For the Eulerian variables which describe the fluid $\mathbf{u}$, p, $\mathbf{f}$; platelets ϕ_{n} and ϕ_{a}; activating chemical c; the cohesion and adhesion stresses and forces $\underline{\underline{\sigma}}^{\mathrm{p}}$, $\underline{\underline{\sigma}}^{\mathrm{w}}$, $\mathbf{f}^{\mathrm{p}}$, and $\mathbf{f}^{\mathrm{w}}$; and the link concentrations z^{p} and z^{w}, we use a uniform mesh placed over R. We take the mesh spacing in both the x and y directions to equal h. Mesh points are denoted $(x_j, y_l) = \big((j-1/2)h, (l-1/2)h\big)$ for $j = 1, \ldots, N_x, l = 1, \ldots, N_y$. Time is discretized into timesteps of size k. We think of the discrete velocity as being defined at time levels $t_{n+1/2} = (n+1/2)k$ and all other variables as being defined at time levels $t_n = nk$. The reason for this is that the 'time-centred' velocities $\mathbf{u}^{n+1/2}$ are involved in the transport of advected quantities between times t_n and t_{n+1}, and the 'time-centred' stresses, e.g. $(\underline{\underline{\sigma}}^{\mathrm{p}})^n$, determine the fluid motion between times $t_{n-1/2}$ and $t_{n+1/2}$. The notation $\mathbf{u}_{jl}^{n+1/2}$ is used for our approximation to the average of the velocity over the h-by-h cell centred at grid point (x_j, y_l) at time $t_{n+1/2}$. Similar notation is used for each of the other Eulerian variables. For each of the partial differential equations which govern the behaviour of an Eulerian variable, we use an appropriate finite-difference approximation defined at points of this mesh. These are described more fully below, as is the discretization of the immersed boundaries.

During each timestep of the computation, we use a fractional step approach to update each of the unknowns. The sequence of updates is as follows:

1. The adhesion and cohesion force densities are calculated from discrete versions of

(4.24) and (4.27) and summed to give their contributions to the fluid force density $\mathbf{f}^n$. Any background force density is also added to $\mathbf{f}^n$.

2. The immersed boundary points are moved (using $\mathbf{u}^{n-1/2}$) and the immersed boundary forces are calculated and transmitted to the fluid grid adding to the fluid force density $\mathbf{f}^n$.
3. The discretized Navier–Stokes equations are solved to give new velocities $\mathbf{u}^{n+1/2}$ and pressure p^n.
4. For each variable ϕ_a, ϕ_n, c, $\underline{\underline{\sigma}}^p$, $\underline{\underline{\sigma}}^w$, z^p, and z^w in turn, the variable is updated to account for advective transport (using $\mathbf{u}^{n+1/2}$) and diffusive transport.
5. The variables ϕ_a, ϕ_n, c, $\underline{\underline{\sigma}}^p$, $\underline{\underline{\sigma}}^w$, z^p, and z^w are updated to account for the reaction terms in their respective transport equations and to yield values at time level $(n+1)k$.

More detailed descriptions of major parts of the numerical methods follows.

5.1 *Solution of Navier–Stokes equations*

The domain from a typical simulation is shown in Fig. 8. Immersed boundaries are used to construct blood vessel walls as described below. We refer to the portion of the computational domain between the walls as the 'vessel'. The computational domain extends upstream and downstream of this 'vessel' to facilitate use of the immersed boundary method to represent the walls. In the region between the vessel walls, we apply a constant background force density $\mathbf{f}^g$ in the x-direction. For flat walls, and in the absence of platelet aggregation, this would result in a parabolic velocity profile between the vessel walls.

Recall that the Navier–Stokes equations are solved in the full rectangular domain, and that the effect of immersed boundaries, platelet–platelet cohesion, and platelet–wall adhesion is felt by the fluid only through the force density $\mathbf{f}$ which appears in the fluid dynamics equations. Thus it is reasonable to use a uniform finite difference grid like that introduced above rather than one that conforms to the geometry of the vessel walls.

To solve the Navier–Stokes equations, we use a second-order approximate projection method similar to that called PMII in Brown *et al.* (2001). In each timestep, the method has two substeps. In the first, a discretization of the momentum equations is used to determine an intermediate velocity field $\mathbf{u}^*$ which is typically not divergence free:

$$\frac{\mathbf{u}^* - \mathbf{u}^{n-1/2}}{k} + \mathbf{a}^n = -Gp^{n-1} + \frac{\nu}{2}\left(L\mathbf{u}^* + L\mathbf{u}^{n-1/2}\right) + \mathbf{f}^n. \tag{5.1}$$

In the second step, $\mathbf{u}^*$ is decomposed into the sum of a divergence free velocity field $\mathbf{u}^{n+1/2}$ and a gradient field $G\phi$ which is used to update the pressure:

$$\mathbf{u}^* = \mathbf{u}^{n+1/2} + kG\phi \tag{5.2}$$

$$p^n = p^{n-1} + kG\phi - \frac{\nu}{2}D \cdot \mathbf{u}^*. \tag{5.3}$$

In the above, G, D, and L are discrete gradient, divergence, and Laplacian operators defined using standard central difference approximations except close to domain boundaries. The term

$$\mathbf{a}^n = \frac{3}{2}(\mathbf{u}^{n-1/2} \cdot G)\mathbf{u}^{n-1/2} - \frac{1}{2}(\mathbf{u}^{n-3/2} \cdot G)\mathbf{u}^{n-3/2}$$

is an approximation at the time nk to the nonlinear advection term $(\mathbf{u} \cdot \nabla)\mathbf{u}$ in the momentum equation. The requirement $D \cdot \mathbf{u}^{n+1/2} = 0$ used with (5.2) would give a discrete Poisson equation $kD \cdot G\phi = D \cdot \mathbf{u}^*$ with a wide ($4h$-by-$4h$) stencil. Instead, because the resulting Navier–Stokes solver has better stability properties, we solve $kL\phi = D \cdot \mathbf{u}^*$ with the standard five-point discrete Laplacian. Therefore, $D \cdot \mathbf{u}^{n+1/2} = 0$ is satisfied only approximately to $O(h^2)$. We note that as part of the projection step (5.2), we calculate cell-edge velocities $u_{j\pm1/2,l}$ on vertical cell edges, and $v_{j,l\pm1/2}$ on horizontal cell edges which satisfy the incompressibility equation

$$u^{n+1/2}_{j+1/2,l} - u^{n+1/2}_{j-1/2,l} + v^{n+1/2}_{j,l+1/2} - v^{n+1/2}_{j,l-1/2} = 0. \tag{5.4}$$

That these cell-edge velocities have this property is important in the algorithm used to advect the Eulerian variables other than $\mathbf{u}$. The boundary conditions for the discrete Navier–Stokes equations are discussed below.

5.2 *Immersed boundary discretization*

The Lagrangian function $\mathbf{X}_i(s, t)$ which describes the ith immersed boundary is represented by a discrete set of points. We use the notation $\mathbf{X}^n_{ip}$ to denote the location of the pth point on the ith immersed boundary at time t_n. Note that these points are *not* constrained to coincide with points of the computational mesh used for the Eulerian variables. Each immersed boundary point moves according to a discrete analogue of (4.29) given by

$$\mathbf{X}^{n+1}_{ip} = \mathbf{X}^n_{ip} + k \sum_{j,l} u^{n+1/2}_{jl} D_{jl}(\mathbf{X}^n_{ip}) h^2. \tag{5.5}$$

Here, $D_{jl}(\mathbf{X})$ denotes the value at grid point (x_j, y_l) of an approximation to the two-dimensional δ-function centred at point $\mathbf{X}$. $D_{jl}(\mathbf{X})$ is described further below. Equation (5.5) shows that each immersed boundary point moves at a velocity that is an average of the fluid velocity at grid points surrounding the immersed boundary point.

At each point $\mathbf{X}_{ip}$, a force is generated by the elastic links that connect that point to other immersed boundary points or tether points (see Fig. 3). For the simulations presented in this paper, we assume that each elastic link satisfies Hooke's law, and so the immersed boundary force at $\mathbf{X}_{ip}$ is given by the expression

$$\mathbf{F}^n_{ip} = \sum_{q \in L_{i,p}} S^{\text{link}}_q (\|\mathbf{X}^n_{ip} - \mathbf{X}^n_{i(q)\,p(q)}\| - R_q) \frac{\mathbf{X}^n_{ip} - \mathbf{X}^n_{i(q)\,p(q)}}{\|\mathbf{X}^n_{ip} - \mathbf{X}^n_{i(q)\,p(q)}\|} + S^{\text{teth}}_{ip} (\mathbf{X}^n_{ip} - \mathbf{X}^{\text{teth}}_{ip}). \tag{5.6}$$

Here, $L_{i,p}$ is the set of indices of links which connect immersed boundary point (i, p) to other immersed boundary points. For $q \in L_{i,p}$, link q connects the immersed boundary point (i, p) to the immersed boundary point $(i(q), p(q))$. S^{link}_q is the stiffness of link q and R_q is its resting length. S^{teth}_{ip} is the stiffness of the link between immersed boundary point (i, p) and its tether point located at $\mathbf{X}^{\text{teth}}_{ip}$. To construct each immersed boundary object included in the present simulations, we use two filaments with equal numbers of

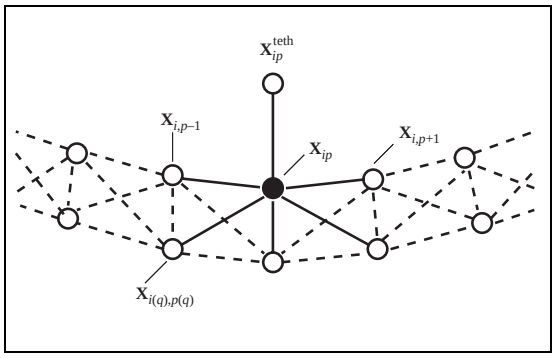

FIG. 3. Immersed boundary representation of walls: link structure in a section of the double filament immersed boundary walls. Solid lines show elastic links from point $\mathbf{X}_{ip}$ to its neighbours $\mathbf{X}_{i(q),p(q)}$ and tether point $\mathbf{X}_{i,p}^{\text{teth}}$. Dashed lines show other elastic links.

immersed boundary points. Each point on a filament is linked to its two neighbouring points on the same filament. As shown in Appendix C, the two terms in the sum in (5.6) which correspond to these connections are a discretization of the tension force expression $(\partial(T\mathbf{t})/\partial s)\ \mathrm{d}s$ in (4.6). Each point is linked also to the corresponding point on the other filament and to the two neighbours of that corresponding point. The resulting criss-cross link structure helps make the immersed boundary structures rigid. The equilibrium separation between the filaments is set to the grid spacing h. Using double filament walls instead of single filament ones also helps isolate the fluid dynamic events in the region of interest (inside the vessel) from those in the rest of the computational domain.

For the simulations presented in this paper, the stiffness constants were set so that the walls would be essentially rigid. Note that the immersed boundary methodology allows for future consideration of more realistic arterial wall mechanics.

The immersed boundary forces given by (5.6) are transmitted to the fluid grid using a discrete analogue of the integral in (4.31):

$$(\mathbf{f}^{\text{ib}})_{jl}^{n} = \sum_{i,p} \mathbf{F}_{ip}^{n} D_{jl}(\mathbf{X}_{ip}^{n}). \tag{5.7}$$

The discrete approximate δ-function $D_{jl}(\mathbf{X})$ used in (5.5) and (5.7) is the one introduced by Peskin (1977). It is constructed from the tensor product of approximate one-dimensional δ-functions $\delta_h(X)$:

$$D_{jl}(X, Y) = \delta_h(X - x_j)\ \delta_h(Y - y_l), \tag{5.8}$$

where

$$\delta_h(x) = \begin{cases} \frac{1}{4h}\ \left(1 + \cos(\frac{\pi x}{2h})\right), & \text{if } |x| \leqslant 2h \\ 0, & \text{otherwise.} \end{cases}$$

It is easily seen that $D_{jl}(\mathbf{X})$ has the property that

$$\sum_{j,l} D_{jl}(\mathbf{X}) h^2 = 1$$

for any point $\mathbf{X}$. Because the support of $D_{jl}(\mathbf{X})$ is confined to a 4×4 portion of the grid surrounding $\mathbf{X}$, the immersed boundary forces are spread by (5.7) to a thin layer of the domain along each immersed boundary, and the average velocity used to move each immersed boundary point in (5.5) is a local average. Many more details about immersed boundary methods can be found in Fauci & Fogelson (1993), and Peskin (1977).

The immersed boundary points and discrete δ-function are also used to define the function $w(\mathbf{x}, t)$ which gives the concentration of reactive sites on the vessel walls. For each immersed boundary, we designate a subset of its points $\mathbf{X}_{ip}$ as reactive. Let I_i denote the set of indices of reactive points on the ith immersed boundary. Then these points make a contribution to the value of w_{jl} at grid point (x_j, y_l) given by the sum

$$w_{jl} = \sum_i \sum_{p \in I_i} W_{ip} D_{jl}(\mathbf{X}_{ip}^n). \tag{5.9}$$

Here, W_{ip} denotes the reactive 'strength' assigned to point $\mathbf{X}_{ip}$. So $w_{jl} \neq 0$ only for points of the grid near reactive portions of the immersed boundaries. In this paper, we simply prescribe at the outset a constant value of the reactive strength W_{ip} for each immersed boundary point, but it is also possible to allow W_{ip} to be determined during the simulation. For example, W_{ip} might depend on the shear stress exerted by the fluid at immersed boundary point $\mathbf{X}_{ip}$.

5.3 *Diffusion*

Platelets and activating chemical are transported by a combination of advection and diffusion. We want to compute solutions to the transport equations using a uniform Cartesian grid over the entire domain, while at the same time limiting the transport to the domain of physical interest between the vessel walls. That is, we want to be sure that there are neither advective nor diffusive fluxes across the immersed boundary walls. In this section we describe how the no-diffusive-flux condition is imposed along these walls. The basic ideas underlying our approach come from the *immersed interface* methods introduced by LeVeque and Li for elliptic problems with discontinuous coefficients (LeVeque & Li, 1994), and extended to elliptic and parabolic problems with Neumann conditions that are imposed along an irregular boundary (Fogelson & Keener, 2000). Here we give the essence of this approach. Further details can be found in the references just cited.

Consider solving the diffusion equation

$$q_t = \beta \Delta q \tag{5.10}$$

in a region Ω^+ bounded by a piecewise-smooth curve Γ along which q satisfies the no-flux condition

$$-\beta \frac{\partial q}{\partial n} = 0. \tag{5.11}$$

We embed the region Ω^+ in a rectangular region Ω and denote by Ω^- the complement of $\overline{\Omega^+}$ in Ω. We extend q to all of Ω by requiring that q satisfy (5.10) in Ω^-, that the extended q be continuous in Ω, and that (5.11) holds along Γ where the derivative is interpreted as a one-sided one involving values of q only on $\Omega^+ \cup \Gamma$. This gives us two interface conditions

$q^+ = q^-$ and $\frac{\partial q}{\partial n}^+ = 0$, and (5.10) implies the third interface condition $(\Delta q)^+ = (\Delta q)^-$. The basic idea of the immersed interface method is to use the regular five-point stencil for the discrete Laplacian at 'regular' grid points away from the interface, and to use the interface conditions to derive a modified stencil for 'irregular' grid points near the interface. An irregular grid point is one for which there is at least one of the regular stencil points on each side of Γ. In choosing the modified stencil we seek to obtain a stable second-order accurate scheme. Because the irregular region is roughly a dimension less than the domain, we achieve pointwise second-order accuracy by constructing an approximate Laplacian at irregular points that is first order.

Consider irregular point $\mathbf{x}_2$ in Fig. 4 and let $\mathbf{x}^*$ be a point on the curve Γ close to $\mathbf{x}_2$ and at which the curve is smooth. Since Δq is continuous in Ω^+, $\Delta q(\mathbf{x}_2) = \Delta q(\mathbf{x}^*)^+ + \mathrm{O}(h)$, so it suffices to approximate $\Delta q(\mathbf{x}^*)^+$ to within $\mathrm{O}(h)$. We approximate $\Delta q(\mathbf{x}^*)^+$ by a linear combination of values of q at the nine mesh points shown by pluses in Fig. 4. It is because $\mathbf{x}^*$ is an interface point that we can use the interface conditions to analyse the accuracy of this approximation and thereby derive appropriate stencil weights. Let K denote the set of indices of these nine points, K^- the subset of indices of points in Ω^-, and K^+ the remaining indices. We seek to determine coefficients γ_k for $k \in K$ so that the truncation error

$$T^* = \Delta q(\mathbf{x}^*)^+ - \sum_{k \in K^+} \gamma_k q(\mathbf{x}_k) - \sum_{k \in K^-} \gamma_k q(\mathbf{x}_k) \tag{5.12}$$

is $\mathrm{O}(h)$. Derivation of equations for these coefficients is facilitated by introducing local orthogonal coordinates (ξ, η) near $\mathbf{x}^*$ as shown in the figure, and assuming that, near $\mathbf{x}^*$, the interface is described by $\xi = \chi(\eta)$. Write $\mathbf{x}_k = (\xi_k, \eta_k)$ and carry out Taylor series expansions about $\mathbf{x}^*$ for each expression in (5.12) in terms of the local coordinates ξ and η:

$$q(\mathbf{x}_k) = q^\pm + q_\xi^\pm \xi_k + q_\eta^\pm \eta_k + \frac{1}{2} q_{\xi\xi}^\pm {\xi_k}^2 + q_{\xi\eta}^\pm \xi_k \eta_k + \frac{1}{2} q_{\eta\eta}^\pm {\eta_k}^2 + \mathrm{O}(h^3). \tag{5.13}$$

Here, each function value or derivative is evaluated using an appropriate one-sided limit from Ω^+ or Ω^- depending on which side of Γ the point $\mathbf{x}_k$ lies. Substituting (5.13) into (5.12), we get an expression for T^* in terms of the 12 quantities $q^\pm$, $q_\xi^\pm$, $q_\eta^\pm$, $q_{\xi\xi}^\pm$, $q_{\xi\eta}^\pm$, and $q_{\eta\eta}^\pm$. The interface conditions allow us to replace the Ω^+ quantities in (5.13) by expressions solely in terms of Ω^- quantities. In terms of the local coordinates (ξ, η), the three interface conditions mentioned above are (i) $q^+ = q^-$, (ii) $q_\xi^+ = 0$, and (iii) $q_{\xi\xi}^+ + q_{\eta\eta}^+ = q_{\xi\xi}^- + q_{\eta\eta}^-$. We obtain three more conditions by taking first and second derivatives with respect to η of the expressions in (i) and the first derivative of the expressions in (ii), evaluating these at $(\xi, \eta) = (0, 0)$, and making use of the facts that $\chi(0) = 0$ and $\chi'(0) = 0$. The three additional conditions are (iv) $q_\eta^+ = q_\eta^-$, (v) $q_{\xi\eta}^+ - \chi'' q_\eta^+ = 0$, and (vi) $q_\xi^+ \chi'' + q_{\eta\eta}^+ = q_\xi^- \chi'' + q_{\eta\eta}^-$. Using the six relations (i)–(vi) we eliminate the quantities q^+, q_ξ^+, q_η^+, $q_{\xi\xi}^+$, $q_{\xi\eta}^+$, and $q_{\eta\eta}^+$ and obtain an expression for T^* in terms of Ω^- quantities. Then to obtain an $\mathrm{O}(h)$ approximation to the Laplacian, we choose the γ_k so that the six terms with q^-, q_ξ^-, q_η^-, $q_{\xi\xi}^-$, $q_{\xi\eta}^-$, and $q_{\eta\eta}^-$ vanish. (Note that we expect $\gamma_k = \mathrm{O}(h^{-2})$ so we must eliminate all six of these terms.) This yields six linear

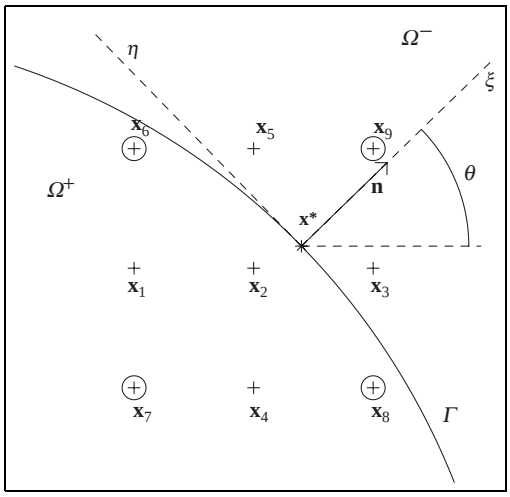

FIG. 4. Stencil for discrete Laplacian at an irregular grid point.

equations for the unknown γ_k, and so, in general, we need six non-zero γ_k, and therefore a six-point stencil, to obtain an $O(h)$ approximation.

To apply these ideas to the solution of the diffusion equation, we use a Crank–Nicolson time discretization, along with the standard five-point discrete Laplacian at regular grid points, and the modified discrete Laplacian just discussed at irregular grid points. In matrix form, this scheme is

$$\left(I - \frac{\beta k}{2} A\right) \mathbf{q}^{n+1} = \left(I + \frac{\beta k}{2} A\right) \mathbf{q}^n \tag{5.14}$$

where the coefficient matrix A corresponds to our approximation to the Laplacian. Thus, for a regular point, the corresponding row of A consists of the coefficients from the standard five-point approximation to the Laplacian, while for an irregular point, the corresponding row of A typically contains six non-zero coefficients determined by solving the six linear equations discussed above. These equations ensure that the local truncation error at each irregular point is $O(h)$. Because there are many possible choices of which six points of the nine point stencil to use, a lot of freedom is left in the choice of γ_k. A sufficient condition for stability of scheme equation (5.14) is that all of the eigenvalues of A lie in the left half of the complex plane or equivalently (since each row sum in A is zero) that each diagonal element of A be negative and each off-diagonal element A be non-negative. In terms of the numbering in Fig. 4, this condition is met if $\{\gamma_2 < 0 \quad \text{and} \quad \gamma_k \geqslant 0 \quad \text{for} \quad k \neq 2\}$. As shown in Fogelson & Keener (2000), this can almost always be achieved by using the usual five-point stencil along with one of the corner points shown by circles in Fig. 4. In the very few cases where no acceptable choice exists, we have seen no sign of instability.

In tests of this method on the diffusion equation, second-order convergence is verified, contours of the solution q intersect the interface Γ orthogonally, and the integral of q over the region of physical interest Ω^+ is conserved to high accuracy.

We use this method to handle the diffusion terms in the equations for ϕ_n and c in the

platelet aggregation model. In this context, the interface Γ consists of the union of the immersed boundary surfaces in direct contact with the blood inside of the vessel. We note that it is straightforward to locate the irregular points by traversing each of these immersed boundary curves and determining where it crosses the computational grid. Also, since in the current simulations the immersed boundaries are tethered strongly and therefore are essentially stationary, the determination of the irregular points and the corresponding stencil coefficients is done only once at the start of a simulation.

5.4 *Advection*

We use a slight modification of LeVeque's high-resolution advection algorithm (LeVeque, 1996) to discretize the advective terms in the transport equations for ϕ_n, ϕ_a, c, $\underline{\underline{\sigma}}^p$, $\underline{\underline{\sigma}}^w$, z^p, and z^w. The method is second-order accurate for smooth q and $\mathbf{u}$, and uses flux-limiters to control oscillations in the numerical solution near discontinuities or steep gradients in q. We briefly describe LeVeque's algorithm and our modification to it to ensure that there is no advective flux across the immersed boundary walls.

LeVeque's algorithm is concerned with solution of a scalar advection equation of the form

$$q_t + \mathbf{u} \cdot \nabla q = 0, \tag{5.15}$$

where the velocity field $\mathbf{u}(\mathbf{x}, t)$ is incompressible. Because $\nabla \cdot \mathbf{u} = 0$, the *advective* form (5.15) can also be written in *conservative* form as

$$q_t + \nabla \cdot (\mathbf{u}q) = 0.$$

These are equivalent for the differential equations, but discretizations based on the advective form are generally different from and often superior to those based on the conservative form. Among the advantages of advective differencing is better treatment of patches of constant q. On the other hand, advective differences may not preserve total mass. For the advection algorithm, q^n_{jl} is interpreted as the cell-average of q over the cell C_{jl} (see Fig. 5). The method uses the cell-edge velocities shown in the figure as well as numerical flux functions $F_{j\pm1/2,l}$ and $G_{j,l\pm1/2}$ which give fluxes of q across the respective cell edges. The final update formula for q is

$$q^{n+1}_{jl} = q^n_{jl} - \tfrac{k}{h}\left\{F_{j+1/2,l} - F_{j-1/2,l} + G_{j,l+1/2} - G_{j,l-1/2}\right\}. \tag{5.16}$$

The version of LeVeque's algorithm that we use proceeds in four steps, the first corresponding to a first-order upwind method, and the later steps giving a series of improvements to this basic method. Each of the steps can be described in terms of waves propagating across the edges of the cells with each wave contributing to the numerical flux of q from one cell to another. The algorithm is a hybrid in that the first step is written in advective form while the correction terms, though based on advective differences, are written in terms of flux differences. The resulting algorithm has the good features of an advective differencing, but is fully conservative provided the discrete incompressibility condition

$$u^{n+1/2}_{j+1/2,l} - u^{n+1/2}_{j-1/2,l} + v^{n+1/2}_{j,l+1/2} - v^{n+1/2}_{j,l-1/2} = 0 \tag{5.17}$$

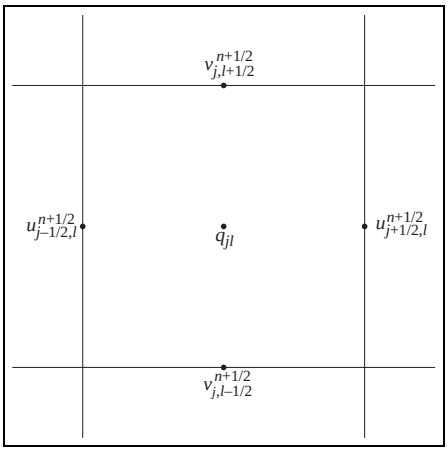

FIG. 5. Advection grid and interface velocities.

holds.

With reference to Fig. 6, we describe the steps involved in updating $\{q^n_{jl}\}$ to $\{q^{n+1}_{jl}\}$. For simplicity, we describe the algorithm as if the velocities u and v are everywhere positive, All of the cell-edge fluxes are initialized to zero.

Step 1 consists of modifying the fluxes by amounts calculated according to the process illustrated in Fig. 6(a). Construct a piecewise constant function with value q^n_{jl} in all of cell C_{jl}. Then $F_{j-1/2,l}$ is modified to account for the *normal* propagation of the value $q^n_{j-1,l}$ from $C_{j-1,l}$ into C_{jl}, and $G_{j,l-1/2}$ is modified to account for the *normal* propagation of the value $q^n_{j,l-1}$ from $C_{j,l-1}$ into C_{jl}. If these were taken as the final values of the fluxes, the resulting method would be a simple first-order upwind procedure.

In each of the remaining steps, the cell-edge fluxes are updated further. Step 2 is also based on the piecewise constant representation of the solution, but takes into account *transverse* propagation across each cell edge as shown in Fig. 6(b). The upward motion of the wave which crosses the cell edge between $C_{j-1,l}$ and C_{jl} affects the cell averages in $C_{j,l}$ and $C_{j,l+1}$ and so adds an increment to the flux $G_{j,l+1/2}$. Similarly, the rightward motion of the wave which crosses the cell edge between $C_{j,l-1}$ and $C_{j,l}$ affects the cell averages in $C_{j,l}$ and $C_{j+1,l}$ and gives an increment to $F_{j+1/2,l}$. If the fluxes after Step 2 were used to update $\{q_{jl}\}$, the method would still be first order but would have a smaller error constant and better stability properties than the simple upwind method.

For Step 3, linear approximations are used to represent the solution in each cell in order to obtain a second-order method. Since the propagation of the cell averages have already been accounted for in Steps 1 and 2, these linear approximations have mean 0. For the propagation in the x-direction, the approximation in cell C_{jl} is linear in x with slope $\frac{1}{h}(q^n_{jl} - q^n_{j-1,l})\,\Phi_{j-1/2,l}$, and is constant in y. The limiter $\Phi_{j-1/2,l}$ is used to prevent the introduction of spurious oscillations or overshoots near steep gradients in q. *Normal* propagation of this linear function from cell $C_{j-1,l}$ into cell C_{jl} modifies $F_{j-1/2,l}$ as shown in Fig. 6(c). Similarly, normal propagation of an approximation to q which in each cell is linear in y and constant in x modifies $G_{j,l-1/2}$. If the fluxes after this step were used to

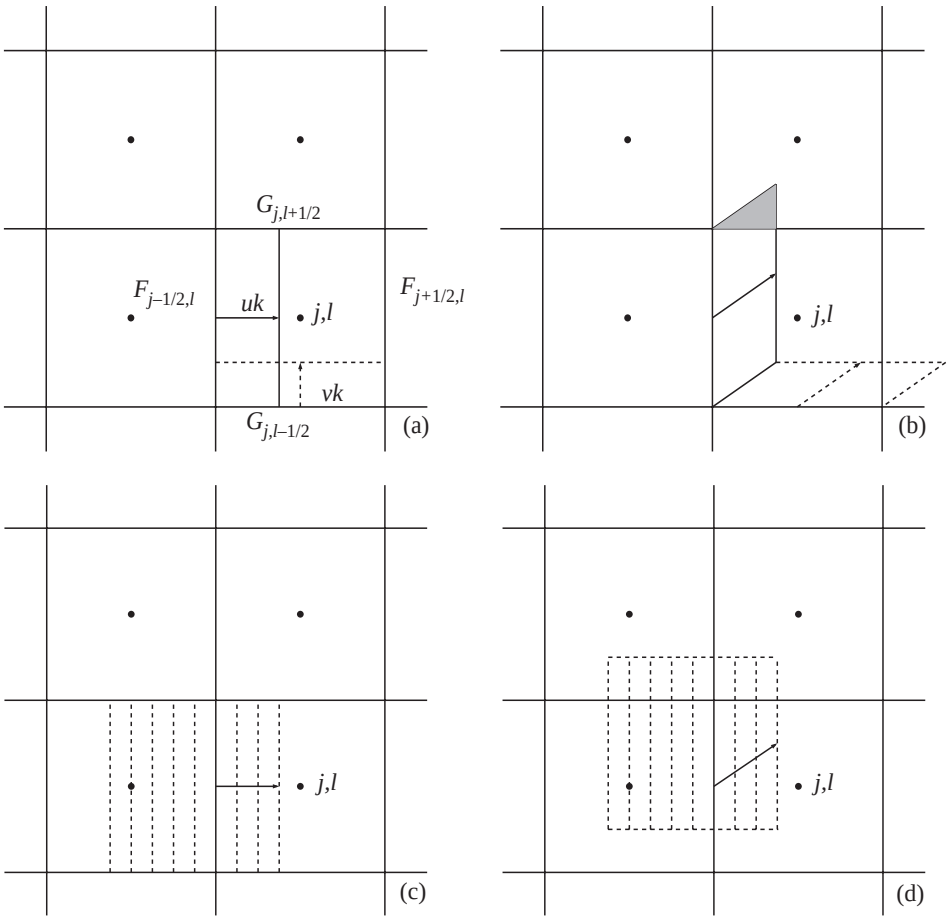

FIG. 6. Geometric picture of LeVeque's advection algorithm. (a) Normal propagation of piecewise constant cell values at speeds $u = u_{j-1/2,l}$ and $v = v_{j,l-1/2}$. (b) Transverse propagation of piecewise constant cell values. (c) Normal propagation of correction wave at speed $u_{j-1/2,l}$. Dashed lines are contours of the linear approximation in cell $C_{j-1,l}$. (d) Transverse propagation of the correction wave with velocity $(u_{j-1/2,l}, v_{j,l+1/2})$.

update $\{q_{jl}\}$, the method would be second-order accurate. LeVeque calls the waves which correspond to Step 3 *correction* waves.

Step 4 accounts for the *transverse* propagation of the correction waves. As shown in Fig. 6(d), the upward motion of the correction wave between cells $C_{j-1,l}$ and C_{jl} affects the fluxes across the top edges of both of these cells and so modifies $G_{j-1,l+1/2}$ and $G_{j,l+1/2}$. In a similar way, the rightward motion of the correction wave between cells $C_{j,l-1}$ and $C_{j,l}$ affects the two fluxes $F_{j+1/2,l-1}$ and $F_{j+1/2,l}$. The transverse propagation of the correction waves does not improve the formal order of accuracy of the method, but can substantially reduce the magnitude of the error. The values $\{q_{jl}^{n+1}\}$ are obtained using these final values of the numerical flux functions in the update formula equation (5.16).

LeVeque's algorithm requires that the discrete incompressibility condition equa-

tion (5.17) be satisfied at time $(n+1/2)k$. As remarked in Section (5.1), cell-edge velocities $u^{n+1/2}_{j\pm1/2,l}$ and $v^{n+1/2}_{j,l\pm1/2}$ which satisfy (5.17) are calculated in the projection step of our Navier–Stokes solver.

We use LeVeque's advection algorithm over the entire grid, and we want to ensure that there is no advective flux across the immersed boundaries that make up the vessel walls. We accomplish this using mask functions $m^x(j,l)$ and $m^y(j,l)$ as follows: by traversing each immersed boundary in contact with the fluid inside the vessel (the same interface Γ on which the no-diffusive-flux condition is imposed), we determine which cell edge midpoints $(x_{j-1/2}, y_l)$ and $(x_j, y_{l-1/2})$ are outside the domain of physical interest, and for these we set $m^x(j,l) = 0$ or $m^y(j,l) = 0$, respectively. For all other horizontal and vertical cell edges, the functions m^x and m^y have value 1. We multiply the cell edge velocities $u_{j-1/2,l}$ and $v_{j,l-1/2}$ by $m^x(j,l)$ and $m^y(j,l)$, respectively, to ensure that the cell edge velocities used by the advection algorithm are 0 for any cell edge outside of the physical domain. Since it is the cell edge velocities that carry material across the edges, this ensures that there is no advective flux across the interface Γ. In tests of the combined advective–diffusion algorithm in a given incompressible velocity field (not shown) second-order convergence was obtained.

5.5 *Reaction terms*

Having accounted for diffusion and advection of the model variables, we now turn to the reaction terms in (a) equations (4.20)–(4.22), (b) equations (4.23) and (4.25), and (c) equations (4.26) and (4.28). In the reaction terms, there is no coupling between different grid points, so our discussion here applies to each grid point (x_j, y_l) separately, and so we drop subscripts jl. We treat separately the reaction terms within each of the three groups notated above and describe each in turn.

The platelet response to the activating chemical ADP is threshold-like (Weiss, 1975), and so we take the activation rate function $R(c)$ in (4.22) to be $R(c) = R_0 H(c - c_T)$ where $H(\cdot)$ is a smoothed version of the Heaviside step function and c_T is the threshold concentration for activation. Within the context of a continuum model, smoothing the activation rate function in this way accounts for the variability of real platelets' sensitivity to the stimulus.

The reaction terms for ϕ_n, ϕ_a, and c give rise to the ordinary differential equations

$$\frac{d\phi_n}{dt} = -\big(R(c) + R^w(w)\big)\phi_n \tag{5.18}$$

$$\frac{d\phi_a}{dt} = \big(R(c) + R^w(w)\big)\phi_n \tag{5.19}$$

$$\frac{dc}{dt} = A\big(R(c^n) + R^w(w)\big)\phi_n(t) - Kc. \tag{5.20}$$

To update, ϕ_n and ϕ_a, we assume that c, and therefore $R(c)$, is constant over the duration of the timestep and we solve analytically the resulting linear differential equations (5.18) and (5.19) to obtain ${\phi_n}^{n+1} = {\phi_n}^n \exp\{-\big(R(c) + R^w(w)\big)k\}$ and ${\phi_a}^{n+1} = {\phi_a}^n + ({\phi_n}^n - {\phi_n}^{n+1})$. Then, we replace $\phi_n(t)$ and $\phi_a(t)$ in (5.20) by their respective averages $({\phi_n}^{n+1} + {\phi_n}^n)/2$ and $({\phi_a}^{n+1} + {\phi_a}^n)/2$, and solve the resulting linear equation analytically to determine c^{n+1}.

The reaction terms in (4.23) and (4.25) give rise to the ordinary differential equations

$$\frac{\mathrm{d}\underline{\underline{\sigma}}^{\mathrm{p}}}{\mathrm{d}t} = \underline{\underline{\sigma}}^{\mathrm{p}}\underline{\underline{\nabla \mathbf{u}}} + (\underline{\underline{\sigma}}^{\mathrm{p}}\underline{\underline{\nabla \mathbf{u}}})^{T} + a_2{\phi_{\mathrm{a}}}^2\underline{\underline{I}} - \beta\left(\frac{\mathrm{Tr}(\underline{\underline{\sigma}}^{\mathrm{p}})}{z^{\mathrm{p}}}\right)\underline{\underline{\sigma}}^{\mathrm{p}} \tag{5.21}$$

$$\frac{\mathrm{d}z^{\mathrm{p}}}{\mathrm{d}t} = a_0{\phi_{\mathrm{a}}}^2 - \beta\left(\frac{\mathrm{Tr}(\underline{\underline{\sigma}}^{\mathrm{p}})}{z^{\mathrm{p}}}\right)z^{\mathrm{p}}. \tag{5.22}$$

Since these are used to determine the cohesion force density $\mathbf{f}^{\mathrm{p}}$ which contributes substantially to determining the fluid motion, stability is a concern, and we found it important to use an implicit (trapezoidal) time discretization of these equations. To describe it, let $\mathcal{A}$ be the operator which computes the time-average of its input at times t_n and t_{n+1}, and let $\underline{\underline{\nabla \mathbf{u}}} = \underline{\underline{\nabla \mathbf{u}}}^{n+1/2}$. Our discretization is

$$\frac{(\underline{\underline{\sigma}}^{\mathrm{p}})^{n+1} - (\underline{\underline{\sigma}}^{\mathrm{p}})^{n}}{k} = \mathcal{A}(\underline{\underline{\sigma}}^{\mathrm{p}})\underline{\underline{\nabla \mathbf{u}}} + \left(\mathcal{A}(\underline{\underline{\sigma}}^{\mathrm{p}})\underline{\underline{\nabla \mathbf{u}}}\right)^{T} + a_2\mathcal{A}(\phi_{\mathrm{a}})^2 - \mathcal{A}\left(\beta\left(\frac{\mathrm{Tr}(\underline{\underline{\sigma}}^{\mathrm{p}})}{z^{\mathrm{p}}}\right)\underline{\underline{\sigma}}^{\mathrm{p}}\right) \tag{5.23}$$

$$\frac{(z^{\mathrm{p}})^{n+1} - (z^{\mathrm{p}})^{n}}{k} = a_0\mathcal{A}(\phi_{\mathrm{a}})^2 - \mathcal{A}\left(\beta\left(\frac{\mathrm{Tr}(\underline{\underline{\sigma}}^{\mathrm{p}})}{z^{\mathrm{p}}}\right)z^{\mathrm{p}}\right). \tag{5.24}$$

The implicit equations are solved iteratively using Newton's method. If a solution is not found after a prescribed number of iterations, we do time-refinement locally at this grid point for these reaction terms. That is, we halve the timestep, and do two steps of half the previous duration in each of which we employ the implicit discretization and iterative solver. If failure is met again, further local time refinement is done. The same procedure is used for the reaction terms in the equations for $\underline{\underline{\sigma}}^{\mathrm{w}}$ and z^{w}.

5.6 *Pressure–flow relation*

Our computational domain represents only a segment of a longer artery, and the pressure drop over the length of the computational domain changes in time because the growing thrombus increases the resistance to flow in this vessel segment. We seek a simple way to account for these facts in our simulations. To this end, consider the situation shown in Fig. 7 in which the portion of the artery corresponding to our computational domain has length L_0 and the remainder of the artery has length ML_0 for some $M \geqslant 0$, so that the length of the complete artery is $(M+1)L_0$.

Imagine that the pressures at the ends of the artery are P_{up} and P_{down} as shown and that the pressure drop $P_{\mathrm{up}} - P_{\mathrm{down}}$ is maintained during a simulation. Before aggregation starts, and ignoring the effect of any stenosis, this pressure drop would drive a steady-state volumetric flow Q_0 related to the pressure drop by the equation $R_0Q_0 = P_{\mathrm{up}} - P_{\mathrm{down}}$. Here, the resistance R_0 is determined from the Poiseuille solution for flow in a channel. Without a stenosis, $R_0 = (M+1)r_0$ where $r_0 = 12\rho\nu L_0/a^3$ is the resistance for a channel of width a and length L_0. Note that, at this time, the pressure drop is identical over any segment of the artery of length L_0.

Now, consider how the situation changes after aggregation begins and there is an increase in resistance to flow within the computational domain because of the aggregate.

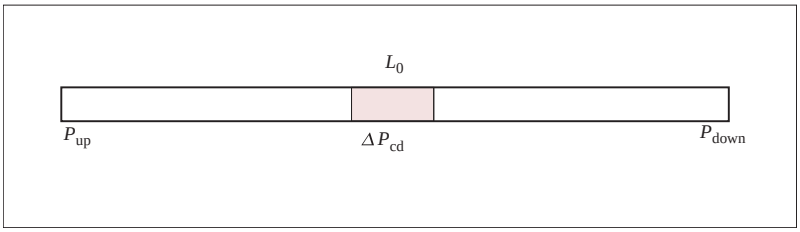

FIG. 7. Schematic of artery which contains computational domain (shaded).

Denote this additional resistance by $R(t)$. (We do not need to know this function explicitly.) Let $\Delta P_{\text{cd}}(t)$ denote the pressure drop over the length of the computational domain at time t, and let $Q(t)$ denote the flow through the domain at that time. (Because of incompressibility, $Q(t)$ is the same for any cross-section of the artery.) The resistance $R(t)$ is defined implicitly by $(r_0 + R(t))Q(t) = \Delta P_{\text{cd}}(t)$. As $R(t)$ grows, both $Q(t)$ and $\Delta P_{\text{cd}}(t)$ change as well, with $Q(t)$ decreasing and $\Delta P_{\text{cd}}(t)$ increasing.

We can determine a relationship between $Q(t)$ and $\Delta P_{\text{cd}}(t)$ if we make the assumption that, for the portion of the artery outside of the computational domain, the pressure–flow relation is that for steady parabolic flow. It then follows that $P_{\text{up}} - P_{\text{down}} - \Delta P_{\text{cd}}(t) = (Mr_0)Q(t)$ and so

$$\Delta P_{\text{cd}}(t) = P_{\text{up}} - P_{\text{down}} - (Mr_0)Q(t). \tag{5.25}$$

This relation is equivalent to

$$P_{\text{up}} - P_{\text{down}} = \big((M+1)r_0 + R(t)\big)Q(t)$$

and, using the relationship satisfied by the initial flow Q_0, $P_{\text{up}} - P_{\text{down}} = \big((M+1)r_0\big)Q_0$, we can write this as

$$\frac{Q(t)}{Q_0} = \frac{(M+1)r_0}{(M+1)r_0 + R(t)}.$$

The larger M is, that is, the longer the artery of which our domain is a piece, the less sensitive the flow $Q(t)$ is to the increased resistance caused by the aggregate. In all cases, however, if the aggregate grows so as to occlude the vessel, $R(t) \to \infty$, $Q(t) \to 0$, and $\Delta P_{\text{cd}}(t) \to P_{\text{up}} - P_{\text{down}}$.

Dividing the terms in (5.25) by the length, L_0, of our computational domain, and defining $g(t) = \Delta P_{\text{cd}}(t)/L_0$ to be the average pressure gradient over the domain, we obtain the formula

$$g(t) = \frac{P_{\text{up}} - P_{\text{down}}}{L_0} - \frac{Mr_0}{L_0}Q(t), \tag{5.26}$$

which we use below.

5.7 *Boundary conditions*

We assume that all variables satisfy periodic boundary conditions in the y-direction, that is, along the top and bottom boundaries in Fig. 8. These boundaries are outside the region of physical interest and the assumption of periodicity simplifies the calculations.

In designing boundary conditions for the upstream and downstream ends of the computational domain, we make use of (5.26) in order to account for the fact that our computational domain is only a piece of a larger artery. We note that if our computational domain is $0 < x < L_0$ and $0 < y < a$, the pressure drop $P_{\mathrm{cd}}(t)$ used above is related to the pointwise pressure $p(x, y, t)$ by

$$P_{\mathrm{cd}}(t) = \frac{1}{a}\left(\int_0^a p(0, y, t)\,\mathrm{d}y - \int_0^a p(L_0, y, t)\,\mathrm{d}y\right)$$

and, similarly, that $Q(t) = \int_0^a u(0, y, t)\,\mathrm{d}y$.

Now, imagine splitting the physical pressure p as $p = \tilde{p} - g(t)x$ where $g(t)$ is given by (5.26). Then the fluid momentum equation (4.18) can be written as

$$\rho(\mathbf{u}_t + \mathbf{u}\cdot\nabla\mathbf{u}) = -\nabla\tilde{p} + g(t)\mathbf{e}_{\mathrm{x}} + \mu\Delta\mathbf{u} + \mathbf{f}^{\mathrm{ib}} + \mathbf{f}^{\mathrm{p}} + \mathbf{f}^{\mathrm{w}}$$

where $\mathbf{e}_{\mathrm{x}}$ is a unit vector in the x-direction and we identify $g(t)\mathbf{e}_{\mathrm{x}}$ with the background force density $\mathbf{f}^{\mathrm{g}}$ in (4.18) which drives flow through the domain. We do a similar splitting of the discrete pressure p^{n-1} and substitute it into the discrete momentum equation (5.1) to obtain

$$\frac{\mathbf{u}^* - \mathbf{u}^{n-1/2}}{k} + \mathbf{a}^n = -G\tilde{p}^{n-1} + g(t_{n-1})\mathbf{e}_{\mathrm{x}} + \frac{\mu}{2}\left(L\mathbf{u}^* + L\mathbf{u}^{n-1/2}\right) + (\mathbf{f}^{\mathrm{ib}})^n + (\mathbf{f}^{\mathrm{p}})^n + (\mathbf{f}^{\mathrm{w}})^n. \tag{5.27}$$

Here $g(t_{n-1})$ can be evaluated as the average of $g(t_{n-3/2})$ and $g(t_{n-1/2})$, and these can be calculated from (5.26) because $\mathbf{u}^{n-3/2}$ and $\mathbf{u}^{n-1/2}$ are known by this time. We define $(\mathbf{f}^{\mathrm{g}})^n = g(t_{n-1})\mathbf{e}_{\mathrm{x}}$. In (5.27), $\tilde{p}$ plays the role of the pressure in the projection method and so values of $\tilde{p}^n$ are obtained from

$$\mathbf{u}^* = \mathbf{u}^{n+1/2} + kG\phi \tag{5.28}$$

$$\tilde{p}^n = \tilde{p}^{n-1} + kG\phi - \frac{\nu}{2}D\cdot\mathbf{u}^*. \tag{5.29}$$

Because $g(t)$ accounts for the pressure drop over the computational domain at time t, it is important that the values of $\tilde{p}$ produced by the projection method satisfy a discrete version of the equation

$$\int_0^a \tilde{p}(0, y, t)\,\mathrm{d}y - \int_0^a \tilde{p}(L_0, y, t)\,\mathrm{d}y = 0. \tag{5.30}$$

Whether they do depends on the boundary conditions imposed on the intermediate velocity $\mathbf{u}^*$ and on ϕ. We require that the x-derivative of both components of $\mathbf{u}^*$ vanish at $x = 0$ and $x = L_0$. These are fairly typical inflow and outflow conditions when the computational domain is only a portion of a longer tube or channel. For ϕ, we require that $\phi(x, y, t) = 0$

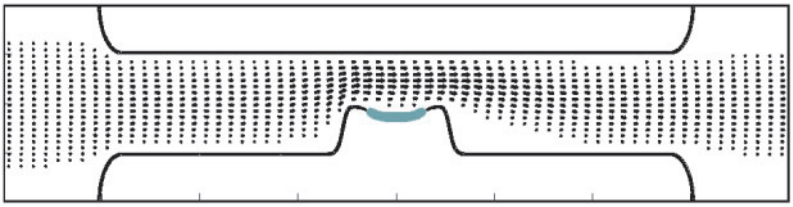

FIG. 8. Computational domain with immersed boundary representation of vessel walls and a 50% stenosis. The equilibrated initial velocity field and the region of damage ($w \neq 0$) are shown. In this and subsequent plots, arrows are shown at every fourth grid point in the x-direction and every second grid point in the y-direction, and arrows for velocities below a prescribed magnitude are not displayed.

at $x = 0$ and $x = L_0$. Using these conditions and the periodicity of the velocity in y, it follows from (5.29) that (5.30) holds at time nk if it holds initially. We note also that the boundary conditions we impose allow the inflow and outflow velocity profiles to adapt to the disturbances produced by the growing aggregate.

In summary, the upstream and downstream boundary conditions we use for the flow variables are that x-derivatives of the velocity vanish, and that the pressure drop over the computational domain between times $t_{n-1/2}$ and $t_{n+1/2}$ is determined from (5.26) using the 'lagged' flow evaluated at time t_{n-1}.

For quantities transported by the fluid, we impose inflow boundary conditions at the upstream end of the vessel segment; typically we set ϕ_{n} to a positive constant, and ϕ_{a}, c, $\underline{\underline{\sigma}}^{\mathrm{p}}$, z^{p}, $\underline{\underline{\sigma}}^{\mathrm{w}}$ and z^{w} to 0. We impose extrapolation outflow boundary conditions on these quantities at the downstream end of the vessel segment. As already noted, our advection and diffusion algorithms were designed to impose conditions of no advective or diffusive flux across the vessel walls themselves.

6. Computational studies

In this section we illustrate the capabilities of the model by showing the results of a variety of computational simulations. Systematic parameter studies will be presented elsewhere. Each simulation is carried out in a stenotic vessel in which up to 50% of the vessel lumen is blocked, see Fig. 8. The vessel is approximately 1 mm in diameter and approximately 6 mm in length. For simulations in each geometry, the initial velocity field is obtained during a preprocessing step. The vessel is considered to be a segment of a longer artery 20 times its length (in the terminology of Section 5.6, $M + 1 = 20$); a pressure drop is prescribed over this longer artery; and the Navier–Stokes equations are solved until the flow equilibrates. The resulting flow has a Reynolds number of about 50 (using $\mu = 0{\cdot}04$ P and $\rho = 1$ g cm^{-3}), and there are recirculation zones adjacent to the upstream and downstream shoulders of the stenosis. A uniform 256×64 grid was used in the calculations.

The geometry used for these simulations is an idealization of a stenosis in which the cap of the plaque has ruptured and exposed platelet-reactive material to the blood. In such situations, the thrombus often begins to form within the plaque itself (Robbie & Libby, 2001) and this is the reason for the 'dip' on top of the stenosis. The 'damaged' tissue is represented by a prescribed non-zero density of reactive wall sites $w(\mathbf{x})$. Platelet interactions with these sites initiates activation and subsequent aggregation.

We present three sets of experiments. The first shows the time development of a thrombus in a stenotic vessel. The second illustrates the importance of considering strain-dependent breaking, by varying the value of β_1 in the breaking rate function given in equation (3.6). The third shows the possibility of embolization.

Figures 9 and 10 show snapshots from a simulation with a 50% stenosis and a moderate value of β_1. The concentration of adhesive and cohesive links, $z^{\mathrm{w}} + z^{\mathrm{p}}$ at each location is shown in dark (low) to light (high) greys to depict the growing aggregate. Locations where the activating chemical's concentration is sufficient to activate platelets are indicated. The velocity field is shown by the arrows; the arrows are scaled identically in all frames so quantitative comparisons can be made between the flows at different times.

Initial activation is induced by interactions of platelets with reactive wall sites, and leads to the release of ADP and subsequent ADP-induced activation. Activated platelets adhere to the reactive wall sites and cohere with one another to begin aggregate formation. Aggregation is initially confined to the dip at the top of the stenosis in which the damaged region is found, and where events are sheltered from the main flow. Because advective transport of non-activated platelets and released ADP is weak in this region, the aggregate grows slowly. While it grows, it also solidifies. This can be seen by the greater extent of the light grey region in the second frame compared to the first.

In the second frame, the aggregate begins to extend out of the downstream end of the dip. Subsequent aggregation is greatly accelerated as ADP is rapidly spread downstream by advection in the faster main flow. This in turn triggers further activation and ADP release, and together these lead to rapid and extensive aggregation downstream of the stenosis. The consequent narrowing of the vessel lumen leads to acceleration of the flow near the upper vessel wall, inducing higher stresses on the top edge of the thrombus and causing increased dissolution of this part of the thrombus via faster link breaking. An approximate steady state is attained in the width of the open lumen above the thrombus and persists through the fourth frame in Fig. 10. In the light grey portions of the thrombus, aggregation has progressed to the extent that these portions behave as a solid and the velocity within them is essentially zero. The dark grey portions of the thrombus are not quite solid and these 'ooze' downstream at a velocity much lower than that of the adjacent free fluid.

Gradually, the aggregate grows out from the upstream end of the damaged region into the stronger flow and this leads to a second period of rapid aggregate growth above the stenosis and to occlusion of the vessel. This is seen in the bottom frame of Fig. 10.

Next, we examine the effect of variations in the sensitivity of the link breaking rate to strain. Recall that we are using a link breaking-rate function, defined in (3.6), in which the breaking rate depends on the local average strain energy $\mathcal{E} = \mathrm{Tr}(\underline{\underline{\sigma}}^{\mathrm{p}})(\mathbf{x})/z^{\mathrm{p}}(\mathbf{x})$. This function is a constant β_0 when $\mathcal{E}$ is not greater than the average energy at which links form $\mathcal{E}_0$, and increases exponentially with $\mathcal{E} - \mathcal{E}_0$ when $\mathcal{E} > \mathcal{E}_0$. The sensitivity of the breaking rate to energies above $\mathcal{E}_0$ is governed by the parameter β_1. We consider four different values of β_1 in a set of simulations in which the geometry (0% stenosis) and all other parameters (including β_0) are held constant. Figure 11 consists of snapshots taken at the same time in these four simulations which show the aggregation intensity (as in the figures above) on the left, and the strain energy per link on the right. From top to bottom, β_1 has value 10, 4, 2, and 0, measured in units of $(\mathcal{E}_0)^{-1}$.

The first thing to notice from the plots of $\mathcal{E}$ is that it is approximately equal to $\mathcal{E}_0$ throughout most of the aggregate. The exceptions are generally on the edge of the aggregate

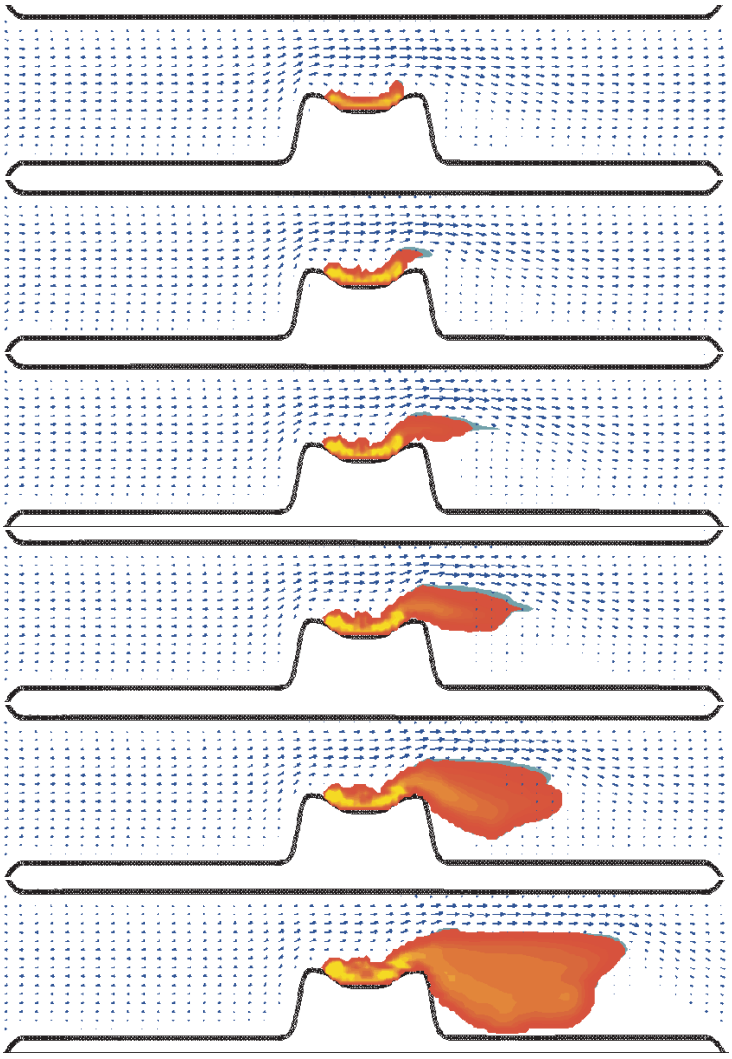

FIG. 9. Thrombus growth in 50% stenosis. Aggregation intensity $z^{\mathrm{p}} + z^{\mathrm{w}}$ (red low, yellow high), above-threshold activating chemical concentration c (grey), velocity field $\mathbf{u}$ (blue vectors).

exposed to the highest fluid shear stress. The maxima of $\mathcal{E}$ in the frames on the right from top to bottom are $1{\cdot}4\,\mathcal{E}_0$, $1{\cdot}9\,\mathcal{E}_0$, $2{\cdot}8\,\mathcal{E}_0$, and $14{\cdot}1\,\mathcal{E}_0$. So, as expected, if links break readily for $\mathcal{E} > \mathcal{E}_0$, that is for large β_1, the aggregate can sustain only values of $\mathcal{E}$ slightly above $\mathcal{E}_0$, while lower values of β_1 allow links to be stretched more without breaking and consequently permit higher values of $\mathcal{E}$ to develop.

A second and surprising observation is that aggregates are larger for higher values of β_1. This is counter to the intuition that if links are more easily broken, the resulting aggregate should be smaller. To understand the observed behaviour, focus on the upstream edge of the aggregate close to the vessel wall as that part of the aggregate forms early in the

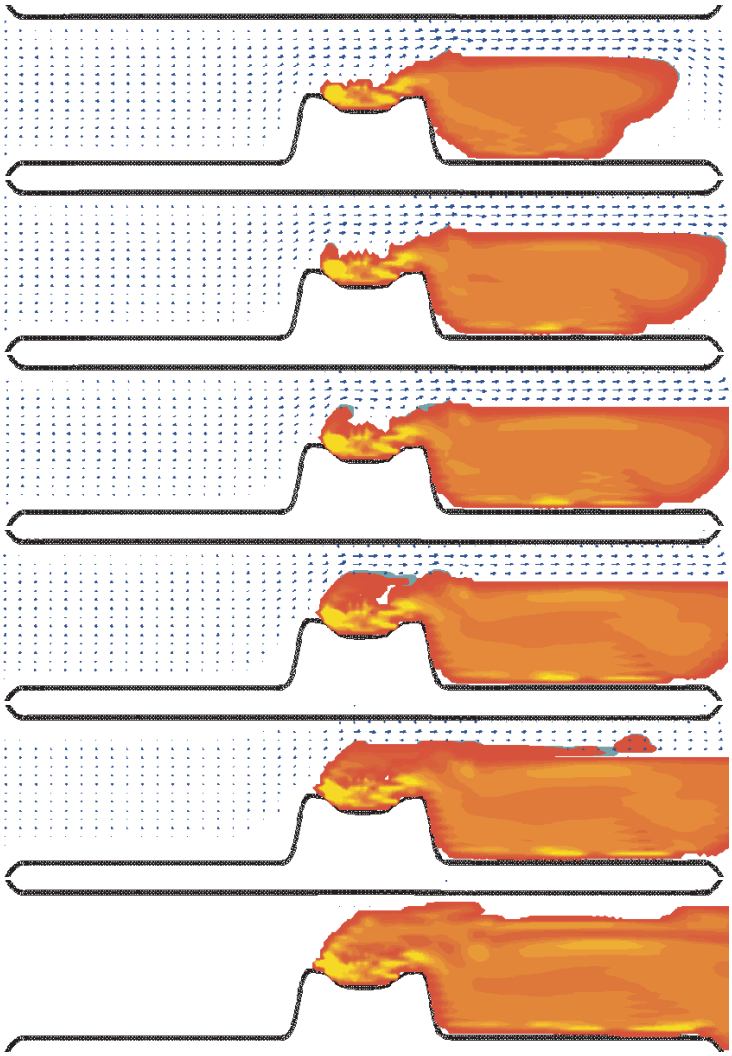

FIG. 10. Thrombus growth in 50% stenosis (continued). Aggregation intensity $z^{\mathrm{p}} + z^{\mathrm{w}}$ (red low, yellow high), above-threshold activating chemical concentration c (grey), velocity field $\mathbf{u}$ (blue vectors).

simulations. In all cases, this part of the aggregate experiences substantial shear stresses as it forms. For the $\beta_1 = 0$ case, the newly formed links can stretch significantly without breaking and can thereby generate forces which prevent further local fluid motion parallel to the wall and which redirect the flow up and over the aggregate. For the $\beta_1 > 0$ cases, similar events occur, but as the links stretch they break at a faster rate. The consequence is that the leading edge of the aggregate is not quite solid and the local fluid motion within it has components both away from and parallel to the wall. The oozing fluid carries with it both platelets activated near the leading edge and ADP released as a consequence of this activation, and thus promotes faster thrombus growth in a direction up and to the right of the

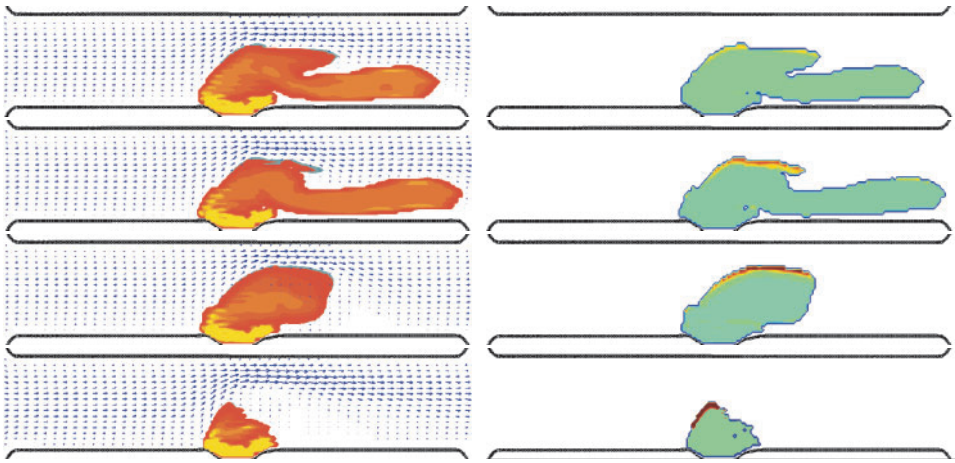

FIG. 11. Effect of link breaking rate. Left: aggregation intensity $z^{\mathrm{p}} + z^{\mathrm{w}}$ (red low, yellow high), and fluid velocity field **u**, (blue vectors). Right: average energy per link $\mathcal{E} = \mathrm{Tr}(\underline{\sigma}^{\mathrm{p}})/z^{\mathrm{p}}$, (green $\approx \mathcal{E}_0$, yellow $\approx 1{\cdot}25\,\mathcal{E}_0$, red greater than $1{\cdot}5\,\mathcal{E}_0$, dark-red greater than $10\,\mathcal{E}_0$). First Row: $\beta_1 = 10$, Second Row: $\beta_1 = 4$, Third Row: $\beta_1 = 2$, Fourth Row: $\beta_1 = 0$. β_1 measured in units of $(\mathcal{E}_0)^{-1}$.

leading edge of the aggregate. This effect becomes more pronounced as β_1 is increased, up to a point. For extremely large β_1, links subject to any strain break rapidly and the aggregate does not hold together. Thus the effect should peak for some value of β_1 and this may be hinted at in the slightly smaller extent of aggregation for $\beta_1 = 10$ (first frame) than for $\beta_1 = 4$ (second frame).

As we just discussed, strain-dependent link breaking can lead to gradual remodelling of an aggregate in response to shear stresses. It can also lead to sudden embolization, in which a large piece of aggregate separates from the wall. This is illustrated in Fig. 12. The results are for a simulation that differs from those above in that the values of β_0 and β_0^{w} are tenfold higher here ($\beta_1 = 4$ as for the simulations shown in Figs 9 and 10). From (2.12), the steady-state link concentration (assuming that all platelets become activated and that $\mathcal{E} < \mathcal{E}_0$) is $z^{\mathrm{p}} = a_0\phi_a^2/\beta_0$ and this suggests that aggregates tend to be weaker for larger values of β_0. In the left frames in Fig. 12, light grey corresponds to a much lower aggregation intensity than it did in the earlier figures.

The top left frame shows an aggregate that, while not quite solid, has substantially reduced the flow velocity compared to that in the free fluid above it. The top right frame shows the average strain energy $\mathcal{E}$. Again there is a layer of high strain energy along the edge of the aggregate that experiences substantial shear stress. There is also a sliver of high strain energy close to where the aggregate is attached to the wall. There is a corresponding sliver of relatively low link concentration in the top left frame. This sliver is a vestige of the manner in which this part of the aggregate formed, which was by folding over of a piece of aggregate initially attached only at the upstream end of the injury.

In the second row of Fig. 12, the left frame shows an increased flow velocity within the aggregate. The right frame shows a remodelling of the upper edge of the aggregate due to stress (the slope of the upstream edge of the aggregate is more gentle than in the frame above), and shows also an increase in the average strain energy near the base of the

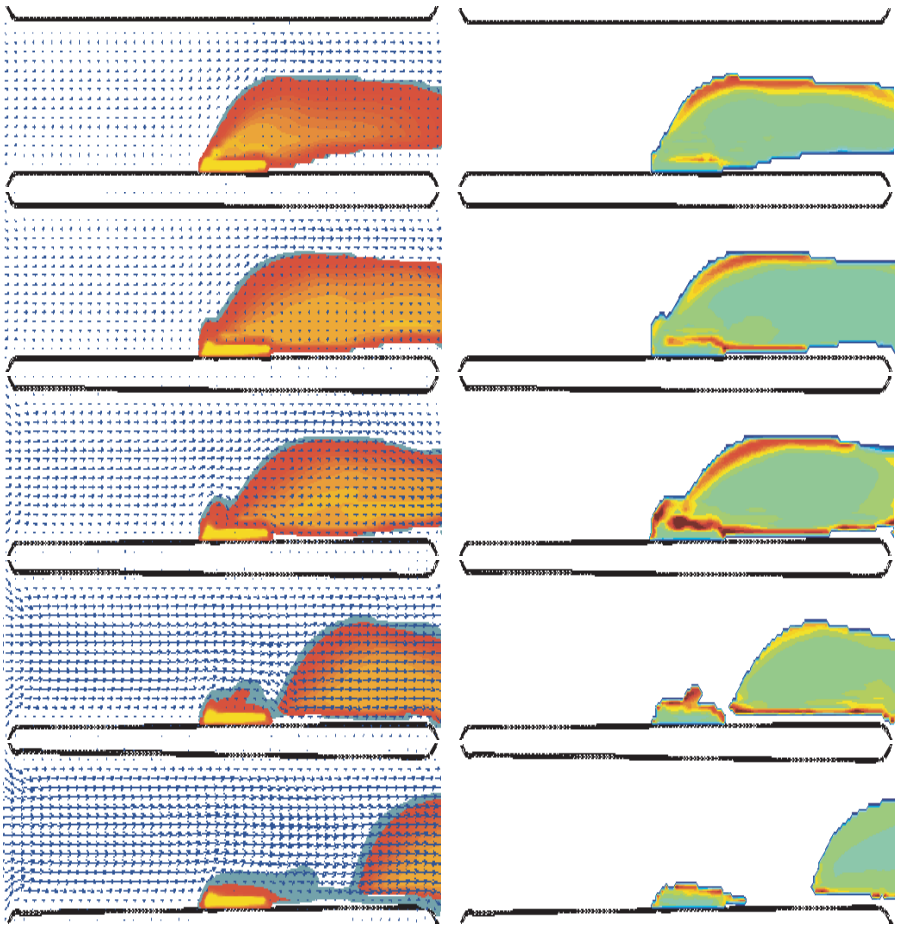

FIG. 12. Embolization. Left: aggregation intensity $z^{\mathrm{p}} + z^{\mathrm{w}}$ (red low, yellow high), above-threshold activating chemical concentration c (grey), and fluid velocity field $\mathbf{u}$, (blue vectors). Right: average energy per link $\mathcal{E} = \mathrm{Tr}(\underline{\underline{\sigma}}^{\mathrm{p}})/z^{\mathrm{p}}$, (green $\approx \mathcal{E}_0$, yellow $\approx 1{\cdot}25\,\mathcal{E}_0$, red greater than $1{\cdot}5\,\mathcal{E}_0$, dark-red greater than $10\,\mathcal{E}_0$).

aggregate. Because higher $\mathcal{E}$ leads to faster link breaking, this process is self-reinforcing and the concentration of links in the 'sliver' is decreased in the next frame while the strain energy is substantially increased. The latter is also due in part to increased relative velocity of the bulk of the aggregate and the piece of aggregate attached to the wall. This process continues and in the next frames we see a large piece of aggregate has broken away from the wall-bound aggregate. In the bottom frames, the separation is greater and the piece of aggregate still attached to the wall has been remodelled because of high stress on portions of its surface. Since there is still substantial ADP in the fluid surrounding the wall-adherent aggregate, growth of another large thrombus is possible, and there could be further cycles of embolization and thrombus growth.

7. Conclusion

Arterial thrombi consist largely of platelet aggregates formed in response to damage to the vessel wall. We have developed a model of the aggregation process that accounts for the influence of fluid motion and forces on aggregation, and for the feedback role of aggregate growth on the fluid dynamics. The model accounts also for the activation of platelets by chemicals in the blood plasma and by vascular tissue exposed through vessel injury. It models platelet–platelet cohesion and now platelet–wall adhesion using evolving distributions of elastic links from which, at any specific time, we can calculate the forces through which the aggregates affect the fluid motion. One of the principal accomplishments described in this paper is the addition of interactions between platelets and the vessel wall to our earlier solution-phase models of aggregation (Fogelson, 1992, 1993). Based on these same earlier models, (Sorensen *et al.*, 1999a,b) presented models of platelet deposition on vessel walls, but their models treated the fluid dynamics as given and allowed no feedback of aggregate development on the flow, or any effect of fluid forces on aggregate growth. Our new model shows the profound disturbances to the flow that can result from growth of aggregates including its complete cessation when a vessel becomes occluded.

A second important achievement of this paper is the development of an approximate closure for the evolution equations that govern the stresses stemming from platelet–platelet cohesion and platelet–wall adhesion. With this closure, we can treat strain-dependent breaking of cohesive and adhesive links without having to explicitly solve for dependence on microscale spatial variables. As the results depicted in Figs 11–12 make clear, strain-dependent link breaking can influence thrombus development through local remodelling of the thrombus' shape and by allowing stress-induced separation of large pieces of an aggregate. Using the computational methods developed in Wang & Fogelson (1999), we could include strain-dependent link breaking in our calculations but only by explicitly treating both macro- and microscale spatial variables. Such computations are two orders of magnitude more costly than those with the closure approximation.

The final important accomplishment reported here is the development of computational methods with which to study the extended model. We described a second-order projection method combined with immersed boundary treatment of the vessel walls that allows us to study flows in vessels of irregular geometry. To impose no-diffusive-flux boundary conditions on the irregular vessel walls for platelet and chemical transport, we use an immersed interface approach to define modified finite-difference stencils near these walls. A high-resolution finite-difference method is used for advective transport; it works well even in the presence of steep concentration gradients. We developed a local time-refinement strategy to improve the stability of computations of the non-advective interactions among the fluid, platelets, and stresses. And we described a pressure-flux boundary condition that allows us to treat the computational domain as a segment of a longer vessel. Elements of the computational methods can be improved, and we are working on these. For example, the outflow boundary conditions for the cohesive stresses sometimes lead to premature termination of a calculation. Local mesh refinement near the stenosis will allow for accurate resolution of the flow at higher Reynolds numbers.

The results presented in this paper illustrate some of the behaviours the model can capture. Systematic study of the model's dependence on parameters, variations in the functional form of the model's kinetic terms, and vessel geometry is needed, as is

comparison with appropriate experimental systems. A particularly nice system for this purpose is the flow chamber, described in Barstad *et al.* (1994), in which a stenosis of defined shape can be incorporated. We are working with two of its authors, Turitto and Sakariassen, to design and carry out a tandem computational and experimental study on aggregation in stenotic artery-sized chambers.

It is also of interest to extend the model, in particular to include other platelet activators. One of these is thrombin which is a potent platelet activator produced on the surface of activated platelets. A simple way to include thrombin in the model is to have activator release be proportional to the concentration of activated platelets (ϕ_a), as was done by Sorensen *et al.* (1999a), rather than having it be proportional to the rate of activation of platelets as is appropriate for ADP. However, this may be too much of a simplification. Thrombin is an enzyme produced by the complex coagulation reaction network, and through feedback reactions can accelerate its own production substantially. Only part of this feedback effect is captured in the assumptions that thrombin induces platelet activation and that the rate of thrombin production is proportional to the concentration of activated platelets. Furthermore, recent modelling (Kuharsky & Fogelson, 2001) and experimental (Hathcock & Nemerson, 2004) results suggest that it may be only the activated platelets near the surface of a thrombus that contribute significantly to thrombin production, and this should be taken into account in adding thrombin to the current model. Another extension of the model would add the possibility of shear-induced platelet activation. There have been many studies (Moake *et al.*, 1988; Alevriadou *et al.*, 1993; Holme *et al.*, 1997) showing that fluid shear stress, in particular high stresses such as those associated with severe stenoses, can activate platelets. It would be straightforward to model an activation mechanism which depends on the instantaneous shear stress experienced by a platelet. It is more difficult to see how, in the context of a continuum model, to model shear-induced activation if it depends on the history of a platelet's exposure to shear stress as has been suggested by Merten *et al.* (2000) and others. We are currently working to include thrombin and shear-stress-induced activation in our models.

Acknowledgments

This work was supported in part by NSF Grants DMS-9307643, DMS-9805518, and DMS-0139926; a Guggenheim Foundation Fellowship to ALF; and an NSF VIGRE grant to the Department of Mathematics at the University of Utah. The authors thank C. Peskin, S. Childress, and R. LeVeque for helpful discussions.

References

ALEVRIADOU, B. R., MOAKE, J. L., TURNER, N. A., RUGGERI, Z. M., FOLIE, B. J., PHILLIPS, M. D., SCHREIBER, A. B., HRINDA, M. E. & MCINTIRE, L. V. (1993) Real-time analysis of shear-dependent thrombus formation and its blockade by inhibitors of von Willebrand factor binding to platelets. *Blood*, **81**, 1263–1276.

ANDERSEN, H., GREENBERG, D. L., FUJIKAWA, K., ZU, W., CHUNG, D. W. & DAVIE, E. W. (1999) Protease-activated receptor 1 is the primary mediator of thrombin-stimulated platelet procoagulant activity. *Proc. Natl Acad. Sci. USA*, **96**, 11189–11193.

ANDRE, P., DELANEY, S., LAROCCA, T., VINCENT, D., DEGUZMAN, F., JUREK, M., KOLLER, B., PHILLIPS, D. & CONLEY, P. (2003) $P2Y_{12}$ regulates platelet adhesion/activation, thrombus growth, and thrombus stability in injured arteries. *J. Clin. Invest.*, **112**, 398–406.

BADIMON, L. & BADIMON, J. J. (1989) Mechanisms of arterial thrombosis in nonparallel streamlines: platelet thrombi grow on the apex of stenotic severely injured vessel wall. Experimental study in the pig model. *J. Clin. Invest.*, **84**, 1134–1144.

BARSTAD, R. M., ROALD, H. E., CUI, Y., TURITTO, V. T. & SAKARIASSEN, K. S. (1994) A perfusion chamber developed to investigate thrombus formation and shear profiles in flowing native human blood at the apex of well-defined stenoses. *Arterioscler. Thromb.*, **14**, 1984–1991.

BATCHELOR, G. K. (1967) *An Introduction to Fluid Dynamics*. Cambridge: Cambridge University Press.

BROWN, D. L., CORTEZ, R. & MINION, M. L. (2001) Accurate projection methods for the incompressible Navier–Stokes equations. *J. Comput. Phys.*, **168**, 464–499.

CANNEGIETER, S. C., RESENDAAL, F. R. & BRIËT, E. (1994) Thromboembolic and bleeding complications in patients with mechanical heart valve prostheses. *Circulation*, **89**, 635–641.

CLEMETSON, K. J. (1995) Platelet activation: signal transduction via membrane receptors. *Thromb. Haemostas.*, **74**, 111–116.

DORSAM, R. T. & KUNAPULI, S. P. (2004) Central role of the $P2Y_{12}$ receptor in platelet activation. *J. Clin. Invest.*, **113**, 340–345.

ESMON, C. T. (1992) The protein C anticoagulant pathway. *Arterioscler. Thromb.*, **12**, 135–145.

FAUCI, L. J. & FOGELSON, A. L. (1993) Truncated Newton methods and the modelling of complex immersed elastic structures. *Commun. Pure Appl. Math.*, **46**, 787–818.

FOGELSON, A. L. (1992) Continuum models of platelet aggregation: formulation and mechanical properties. *SIAM JAM*, **52**, 1089–1110.

FOGELSON, A. L. (1993) Continuum models of platelet aggregation: mechanical properties and chemically-induced phase transitions. *Contemp. Math.*, **141**, 279–294.

FOGELSON, A. L. & KEENER, J. P. (2000) Immersed interface methods for Neumann and related problems in two and three dimensions. *SIAM J. Sci. Comput.*, **22**, 1630–1654.

FORRESTER, J., LITVACK, F., GRUNDFEST, W. & HICKEY, A. (1987) A perspective of coronary disease seen through the arteries of living man. *Circulation*, **75**, 6–14.

FUSTER, V., BADIMON, L., COHEN, M., AMBROSE, J., BADIMON, J. & CHESEBRO, J. (1988) Insights into the pathogenesis of acute ischemic syndromes. *Circulation*, **77**, 15–22.

GOLDSMITH, H. L. & KARINO, T. (1977) Microscopic considerations: the motions of individual particles. *Annals of the New York Academy of Sciences*, Vol. 283. (L. Vroman & E. Leonard, eds). New York: New York Academy of Sciences, pp. 241–255.

GRABOWSKI, E., FRANTA, J. & DIDISHEIM, P. (1978) Platelet aggregation in flowing blood *in vitro* II. Dependence of aggregate growth rate on ADP concentration and shear rate. *Microvasc. Res.*, **16**, 183–195.

GRABOWSKI, E., FRIEDMAN, L. & LEONARD, E. (1972) Effects of shear rate on the diffusion and adhesion of blood platelets to a foreign surface. *Ind. Engng Chem. Fund.*, **11**, 224–232.

GUY, R. D. (2004) *Continuum models of platelet aggregation: closure models, computational methods, and simulation.* Ph.D. Thesis, University of Utah, Salt Lake City, Utah.

HATHCOCK, J. J. & NEMERSON, Y. (2004) Platelet deposition inhibits tissue factor activity: *in vitro* clots are impermeable to factor Xa. *Blood*, **104**, 123–127.

HOLME, P. A., ORVIM, U., HAMERS, M. J. A. G., SOLUM, N. O., BROSSTAD, F. R., BARSTAND, R. M. & SAKARIASSEN, K. S. (1997) Shear-induced platelet activation and platelet microparticle formation at blood flow conditions as in arteries with a severe stenosis. *Arterioscler. Thromb. Vasc. Biol.*, **17**, 646–653.

KARINO, T. & GOLDSMITH, H. L. (1980) Disturbed flow in models of branching vessels. *Trans. Am. Soc. Artif. Intern. Organs*, **XXVI**, 500–506.

KARINO, T. & MOTOMIYA, M. (1984) Flow through a venous valve and its implication for thrombus formation. *Thrombosis Research*, **36**, 245–257.

KUHARSKY, A. L. & FOGELSON, A. L. (2001) Surface-mediated control of blood coagulation: the role of binding site densities and platelet deposition. *Biophys. J.*, **80**, 1050–1074.

LAGES, B. (1986) In vitro platelet responses: Dense granule secretion. *Platelet Responses and Metabolism Vol. I: Responses*. (H. Holmsen, ed.). Boca Raton, FL: CRC Press, pp. 115–143.

LEVEQUE, R. J. (1996) High-resolution conservative algorithms for advection in incompressible flow. *SIAM J. Numer. Anal.*, **33**, 627–665.

LEVEQUE, R. J. & LI, Z. (1994) The immersed interface method for elliptic equations with discontinuous coefficients and singular sources. *SIAM J. Numer. Anal.*, **31**, 1019–1044.

MANN, K. G. & LORAND, L. (1993) Introduction: blood coagulation. *Methods Enzymol.*, **222**, 1–10.

MARCUS, A. J. & SAFIER, L. B. (1993) Thromboregulation: multicellular modulation of platelet reactivity in hemostasis and thrombosis. *FASEB J.*, **7**, 516–522.

MARGUERIE, G., GINSBERG, M. & PLOW, E. (1986) Glycoproteins: the fibrinogen receptor. *Platelet Responses and Metabolism Vol. III: Response–Metabolism Relationships*. Boca Raton, FL: CRC Press, pp. 285–296.

MERTEN, M., CHOW, T., HELLUMS, J. D. & THIAGARAJAN, P. (2000) A new role for P-selectin in shear-induced platelet aggregation. *Circulation*, **102**, 2045–2050.

MOAKE, J. L., TURNER, N. A., STATHOPOULOS, N. A., NOLASCO, L. & HELLUMS, J. D. (1988) Shear-induced platelet aggregation can be mediated by vWF released from platelets, as well as by exogenous large or unusually large vWF multimers, requires adenosine diphosphate, and is resistant to aspirin. *Blood*, **71**, 1366–1374.

MOHAMMAD, S. F. (1995) Platelet adhesion to damaged vessel wall. *Principles of Cell Adhesion*. (P. Richardson & M. Steiner, eds). Boca Raton, FL: CRC Press.

PESKIN, C. S. (1977) Numerical analysis of blood flow in the heart. *J. Comput. Phys.*, **25**, 220–252.

PESKIN, C. S. & MCQUEEN, D. M. (1980) Modeling prosthetic heart valves for numerical analysis of blood flow in the heart. *J. Comput. Phys.*, **37**, 113–132.

PESKIN, C. S. & MCQUEEN, D. M. (1993) Computational biofluid dynamics. *Contemp. Math.*, **141**, 161–186.

PHAN-THIEN, N. & TANNER, R. (1977) A new constitutive equation derived from network theory. *J. Non-Newtonian Fluid Mech.*, **2**, 353–365.

ROBBIE, L. & LIBBY, P. (2001) Inflammation and atherosclerosis. *Annals of the New York Academy of Sciences*, Vol. 947. (F. Numano & M. A. Gimbrone Jr, eds). New York: New York Academy of Sciences, pp. 167–179.

RUGGERI, Z. M. (1997) Mechanisms initiating platelet thrombus formation. *Thromb. Haemostas.*, **78**, 611–616.

SORENSEN, E. N., BURGREEN, G. W., WAGNER, W. R. & ANTAKI, J. F. (1999a) Computational simulation of platelet deposition and activation: I. Model development and properties. *Ann. Biomed. Engng*, **27**, 436–448.

SORENSEN, E. N., BURGREEN, G. W., WAGNER, W. R. & ANTAKI, J. F. (1999b) Computational simulation of platelet deposition and activation: II. Results for Poiseuille flow over collagen. *Ann. Biomed. Engng*, **27**, 449–458.

TURITTO, V. T. & BAUMGARTNER, H. R. (1975) Platelet interaction with subendothelium in a perfusion system. *Microvasc. Res.*, **9**, 335–344.

TURITTO, V. T., BENIS, A. & LEONARD, E. (1972) Platelet diffusion in flowing blood. *Ind. Engng*

Chem. Fund., **11**, 216–223.

TURITTO, V. T. & WEISS, H. J. (1979) Rheological factors influencing platelet interactions with vessel surfaces. *J. Rheology*, **23**, 735.

WANG, N. & KELLER, K. (1985) Augmented transport of extracellular solutes in concentrated erythrocyte suspensions in couette flow. *J. Colloid Interface Sci.*, **103**, 210–225.

WANG, N. T. & FOGELSON, A. L. (1999) Computational methods for continuum models of platelet aggregation. *J. Comput. Phys.*, **151**, 649–675.

WEISS, H. J. (1975) Platelet physiology and abnormalities of platelet function (Part 1). *New Engl. J. Med.*, **293**, 531–541.

WHITE, J. G. (1994) Anatomy and structural organization of the platelet. *Hemostasis and Thrombosis: Basic Principles and Clinical Practice*. (R. W. Colman, J. Hirsh, V. J. Marder & E. W. Salzman, eds). Philadelphia, PA: Lippincott, pp. 397–413.

Appendix A. Derivation of transport equation for $E(\mathbf{x}, \mathbf{y}, t)$

To derive the transport equation (2.7) for the platelet–platelet link distribution functions $E(\mathbf{x}, \mathbf{y}, t)$, we consider the *total* number $N(t)$ of elastic links between activated platelets in an arbitrary material volume $\Omega_x(t)$ and those in an arbitrary material volume $\Omega_\xi(t)$:

$$N(t) = \int_{\Omega_x(t)} \int_{\Omega_\xi(t)} \widetilde{E}(\mathbf{x}, \boldsymbol{\xi} - \mathbf{x}, t)\, \mathrm{d}\boldsymbol{\xi}\, \mathrm{d}\mathbf{x}.$$

We assume that $N(t)$ changes only because new links form and existing links break, and that these reactions obey mass action kinetics. Therefore,

$$\frac{\mathrm{d}N(t)}{\mathrm{d}t} = \int_{\Omega_x(t)} \int_{\Omega_\xi(t)} \left\{ \widetilde{\alpha}(|\boldsymbol{\xi} - \mathbf{x}|)\phi_a(\boldsymbol{\xi}, t)\phi_a(\mathbf{x}, t) \; - \; \widetilde{\beta}(|\boldsymbol{\xi} - \mathbf{x}|)\widetilde{E}(\mathbf{x}, \boldsymbol{\xi} - \mathbf{x}, t) \right\} \mathrm{d}\boldsymbol{\xi}\, \mathrm{d}\mathbf{x}. \tag{A.1}$$

Here, $\widetilde{\alpha}$ and $\widetilde{\beta}$ are the link formation and breaking rates, respectively. To derive an expression for $\mathrm{d}N/\mathrm{d}t$ from the definition of $N(t)$, we proceed in a way standard in continuum mechanics. Let $\varphi(\mathbf{x}_0, t)$ denote the flow map. That is, $\mathbf{x} = \varphi(\mathbf{x}_0, t)$ gives the location at time t of the fluid particle which is at location $\mathbf{x}_0$ at time 0. Suppose $\Omega_x(0)$ and $\Omega_\xi(0)$ are the respective preimages of the regions $\Omega_x(t)$ and $\Omega_\xi(t)$ under the flow map, and let $J(\mathbf{x}_0, t)$ denote the Jacobian of the flow map evaluated at point $\mathbf{x}_0$. Then, we change variables from $\mathbf{x}$ and $\boldsymbol{\xi}$ to $\mathbf{x}_0$ and $\boldsymbol{\xi}_0$ in the integrals defining $N(t)$ to get

$$N(t) = \int_{\Omega_x(0)} \int_{\Omega_\xi(0)} \widetilde{E}(\mathbf{x}(t), \boldsymbol{\xi}(t) - \mathbf{x}(t), t)\, J(\mathbf{x}_0, t)\, J(\boldsymbol{\xi}_0, t)\, \mathrm{d}\boldsymbol{\xi}_0\, \mathrm{d}\mathbf{x}_0, \tag{A.2}$$

where we have used the notation $\mathbf{x}(t) = \varphi(\mathbf{x}_0, t)$ and $\boldsymbol{\xi}(t) = \varphi(\boldsymbol{\xi}_0, t)$. Since the integral is now over a domain fixed in time, it is straightforward to compute the time derivative of

$N(t)$ to be

$$\frac{dN}{dt} = \int_{\Omega_x(0)} \int_{\Omega_\xi(0)} \left\{ \frac{\partial \widetilde{E}}{\partial t} + \frac{d\mathbf{x}}{dt} \cdot \nabla_1 \widetilde{E} + \left(\frac{d\boldsymbol{\xi}}{dt} - \frac{d\mathbf{x}}{dt} \right) \cdot \nabla_2 \widetilde{E} \right\} J(\mathbf{x}_0, t) J(\boldsymbol{\xi}_0, t) \, d\boldsymbol{\xi}_0 \, d\mathbf{x}_0$$
$$+ \int_{\Omega_x(0)} \int_{\Omega_\xi(0)} \left\{ \widetilde{E} \frac{\partial J(\mathbf{x}_0, t)}{\partial t} J(\boldsymbol{\xi}_0, t) \right\} d\boldsymbol{\xi}_0 \, d\mathbf{x}_0$$
$$+ \int_{\Omega_x(0)} \int_{\Omega_y(0)} \left\{ \widetilde{E} J(\mathbf{x}_0, t) \frac{\partial J(\boldsymbol{\xi}_0, t)}{\partial t} \right\} d\boldsymbol{\xi}_0 \, d\mathbf{x}_0. \tag{A.3}$$

Here, ∇_i denotes the gradient of $\widetilde{E}$ with respect to its ith argument. Now, $d\mathbf{x}/dt = \mathbf{u}(\mathbf{x}(t), t)$, and it follows that, for any $\mathbf{x}_0$,

$$\frac{\partial J}{\partial t}(\mathbf{x}_0, t) = J(\mathbf{x}_0, t) \, \nabla \cdot \mathbf{u}(\mathbf{x}(t), t).$$

Since the flow is incompressible, $\nabla \cdot \mathbf{u} = 0$, and so $J_t(\mathbf{x}_0, t) = 0$ for all $\mathbf{x}_0$. Hence, the second and third integrals in (A.3) vanish, to leave

$$\frac{dN}{dt} = \int_{\Omega_x(0)} \int_{\Omega_\xi(0)} d\boldsymbol{\xi}_0 \, d\mathbf{x}_0 \, J(\mathbf{x}_0, t) J(\boldsymbol{\xi}_0, t)$$
$$\times \left(\frac{\partial \widetilde{E}}{\partial t} + \mathbf{u}(\mathbf{x}(t), t) \cdot \nabla_1 \widetilde{E} + (\mathbf{u}(\boldsymbol{\xi}(t), t) - \mathbf{u}(\mathbf{x}(t), t)) \cdot \nabla_2 \widetilde{E} \right).$$

In this expression, the arguments of $\widetilde{E}$ are $\mathbf{x}(t)$, $\boldsymbol{\xi}(t) - \mathbf{x}(t)$, and t. Now change variables from $\mathbf{x}_0$ and $\boldsymbol{\xi}_0$ back to $\mathbf{x}$ and $\boldsymbol{\xi}$, to obtain

$$\frac{dN}{dt} = \int_{\Omega_x} \int_{\Omega_\xi} d\boldsymbol{\xi} \, d\mathbf{x} \left(\frac{\partial \widetilde{E}}{\partial t} + \mathbf{u}(\mathbf{x}, t) \cdot \nabla_1 \widetilde{E} + (\mathbf{u}(\boldsymbol{\xi}, t) - \mathbf{u}(\mathbf{x}, t)) \cdot \nabla_2 \widetilde{E} \right). \tag{A.4}$$

Equating this to the expression for dN/dt in (A.1), noting that the integrands must match because the regions of integration are arbitrary, and then letting $\mathbf{r} = \boldsymbol{\xi} - \mathbf{x}$, we conclude that

$$\frac{\partial \widetilde{E}}{\partial t} + \mathbf{u}(\mathbf{x}, t) \cdot \nabla_x \widetilde{E} + (\mathbf{u}(\mathbf{x} + \mathbf{r}, t) - \mathbf{u}(\mathbf{x}, t)) \cdot \nabla_r \widetilde{E} = \widetilde{\alpha}(|\mathbf{r}|) \phi_a(\mathbf{x}, t) \phi_a(\mathbf{x} + \mathbf{r}, t) - \widetilde{\beta}(|\mathbf{r}|) \widetilde{E}. \tag{A.5}$$

Note that the expression on the left is exactly what we would have obtained if we applied the chain rule to $\widetilde{E}(\mathbf{x}(t), \boldsymbol{\xi}(t) - \mathbf{x}(t), t)$.

The platelet length scale is much smaller than the macroscopic length scale, so we expect $\widetilde{\alpha}$, $\widetilde{\beta}$, and $\widetilde{E}$ to vary rapidly with the separation vector $\mathbf{r}$. To make this explicit, let $\mathbf{r} = \epsilon \mathbf{y}$, and define $\alpha(|\mathbf{y}|) = \epsilon^3 \widetilde{\alpha}(\mathbf{r})$, $\beta(|\mathbf{y}|) = \beta(\mathbf{r})$, and $E(\mathbf{x}, \mathbf{y}, t) = \epsilon^3 \widetilde{E}(\mathbf{x}, \mathbf{r}, t)$. Finally, expand $\mathbf{u}(\mathbf{x} + \epsilon \mathbf{y}, t)$ and $\phi_a(\mathbf{x} + \epsilon \mathbf{y}, t)$ about $\mathbf{x}$ and keep only the O(1) terms to obtain

$$\frac{\partial E}{\partial t} + \mathbf{u}(\mathbf{x}, t) \cdot \nabla_x E + (\mathbf{y} \cdot \nabla \mathbf{u}) \cdot \nabla_y E = \alpha(|\mathbf{y}|) \phi_a(\mathbf{x}, t)^2 - \beta(|\mathbf{y}|) E \tag{A.6}$$

which is the form of the equation used in the model.

Appendix B. Derivation of formulae for $\mathbf{f}^{\mathrm{p}}$ and $\mathbf{f}^{\mathrm{w}}$

To derive (2.8), we begin with the expression for the total body force at point $\mathbf{x}$ generated by links between activated platelets there and activated platelets at other points:

$$\mathbf{f}^{\mathrm{p}}(\mathbf{x}, t) = \int \widetilde{E}(\mathbf{x}, \mathbf{r}, t)\widetilde{\mathbf{F}}(\mathbf{r})\, \mathrm{d}\mathbf{r} \tag{B.1}$$

where $\widetilde{\mathbf{F}}(\mathbf{r})$ is the force generated by a single link. In terms of the scaled coordinate $\mathbf{y} = \mathbf{r}/\epsilon$, the force $\mathbf{F}(\mathbf{y})$ is defined so that $\widetilde{\mathbf{F}}(\mathbf{r}) = \epsilon^{-1}\mathbf{F}(\mathbf{y})$. The factor ϵ^{-1} accounts for the rescaling of the length dimension in the force. With this change of variables,

$$\mathbf{f}^{\mathrm{p}} = \epsilon^{-1} \int E(\mathbf{x}, \mathbf{y}, t)\mathbf{F}(\mathbf{y})\, \mathrm{d}\mathbf{y}. \tag{B.2}$$

As we show, the factor ϵ^{-1} is not a problem because the integrand is nearly an odd function of $\mathbf{y}$, and so the body force is order one. Clearly $\mathbf{F}(\mathbf{y})$ is an odd function. The link function $E(\mathbf{x}, \mathbf{y}, t)$ is not, but must satisfy the equation

$$E(\mathbf{x}, -\mathbf{y}, t) = E(\mathbf{x} - \epsilon\mathbf{y}, \mathbf{y}, t) \tag{B.3}$$

because both expressions describe the concentrations of links between platelets at the points $\mathbf{x}$ and $\mathbf{x} - \epsilon\mathbf{y}$. Expanding the right side of this equation for small ϵ gives

$$E(\mathbf{x}, -\mathbf{y}, t) = E(\mathbf{x}, \mathbf{y}, t) - \epsilon\mathbf{y} \cdot \nabla_x E(\mathbf{x}, \mathbf{y}, t) + \mathcal{O}(\epsilon^2). \tag{B.4}$$

We make the change of variables $\mathbf{y} \to -\mathbf{y}$ in (B.2) and we use the expansion (B.4) and the fact that $\mathbf{F}(-\mathbf{y}) = -\mathbf{F}(\mathbf{y})$ to obtain

$$\mathbf{f}^{\mathrm{p}}(\mathbf{x}, t) = -\mathbf{f}^{\mathrm{p}}(\mathbf{x}, t) + \int \mathbf{y} \cdot \nabla_x E(\mathbf{x}, \mathbf{y}, t)\mathbf{F}(\mathbf{y})\, \mathrm{d}\mathbf{y} + \mathcal{O}(\epsilon). \tag{B.5}$$

We rearrange this equation, retain only the leading order term, and write $\mathbf{F}(\mathbf{y}) = S(|\mathbf{y}|)\mathbf{y}$ to obtain

$$\mathbf{f}^{\mathrm{p}}(\mathbf{x}, t) = \frac{1}{2} \int \mathbf{y} \cdot \nabla_x E(\mathbf{x}, \mathbf{y}, t) S(|\mathbf{y}|)\mathbf{y}\, \mathrm{d}\mathbf{y} \tag{B.6}$$

which is the expression in (2.8).

The derivation of the formula (B.8) for $\mathbf{f}^{\mathrm{w}}$ is similar to but not the same as that just given because $E^{\mathrm{w}}(\mathbf{x}, \mathbf{y}, t)$ does not have the 'almost-odd' character of $E(\mathbf{x}, \mathbf{y}, t)$. The adhesive force density $\mathbf{f}^{\mathrm{w}}(\mathbf{x}, t)$ at $\mathbf{x}$ is the resultant of (i) the net force from elastic links which connect activated platelets near $\mathbf{x}$ to sticky wall sites elsewhere, and (ii) the net force from elastic links which connect sticky wall sites near $\mathbf{x}$ with activated platelets elsewhere. Thus,

$$\mathbf{f}^{\mathrm{w}}(\mathbf{x}, t) = \int \widetilde{E}^{\mathrm{w}}(\mathbf{x}, \mathbf{r}, t)\widetilde{\mathbf{F}}^{\mathrm{w}}(\mathbf{r})\, \mathrm{d}\mathbf{r} + \int \widetilde{E}^{\mathrm{w}}(\mathbf{x} - \mathbf{r}, \mathbf{r}, t)\widetilde{\mathbf{F}}^{\mathrm{w}}(-\mathbf{r})\, \mathrm{d}\mathbf{r} \tag{B.7}$$

where $\widetilde{\mathbf{F}}^{\mathrm{w}}(\mathbf{r})$ is the force generated by a single adhesive link. We make the change of variables $\mathbf{r} = \epsilon\mathbf{y}$ in both integrals. We recall that $E^{\mathrm{w}}(\mathbf{x}, \mathbf{y}, t) = \epsilon^3 \widetilde{E}^{\mathrm{w}}(\mathbf{x}, \mathbf{r}, t)$, we define

$\mathbf{F}^{\mathrm{w}}(\mathbf{y})$ by $\widetilde{\mathbf{F}}^{\mathrm{w}}(\mathbf{r}) = \epsilon^{-1}\mathbf{F}^{\mathrm{w}}(\mathbf{y})$, and we assume that $\mathbf{F}^{\mathrm{w}}(\mathbf{y}) = S^{\mathrm{w}}(|\mathbf{y}|)\mathbf{y}$. With these changes, we have

$$\mathbf{f}^{\mathrm{w}}(\mathbf{x}, t) = \epsilon^{-1} \int \{E^{\mathrm{w}}(\mathbf{x}, \mathbf{y}, t) - E^{\mathrm{w}}(\mathbf{x} - \epsilon\mathbf{y}, \mathbf{y}, t)\}\, S^{\mathrm{w}}(|\mathbf{y}|)\mathbf{y}\, \mathrm{d}\mathbf{y}.$$

We expand $E^{\mathrm{w}}(\mathbf{x} - \epsilon\mathbf{y}, \mathbf{y}, t)$ in a Taylor series in its first argument about the point $\mathbf{x}$, substitute this into the above integral, and obtain to the leading order in ϵ

$$\mathbf{f}^{\mathrm{w}}(\mathbf{x}, t) = \int \mathbf{y} \cdot \nabla E^{\mathrm{w}}(\mathbf{x}, \mathbf{y}, t) S^{\mathrm{w}}(|\mathbf{y}|)\mathbf{y}\, \mathrm{d}\mathbf{y}. \tag{B.8}$$

Appendix C. Immersed boundary forces

The terms in the sum in (5.6) which give the force on immersed boundary point $\mathbf{X}_{ip}$ generated by the connections between it and its two neighbouring points on the same immersed boundary (see Fig. 3) have the form

$$S^{\mathrm{link}}(\|\mathbf{X}_{ip} - \mathbf{X}^n_{i,p+1}\| - R)\frac{\mathbf{X}_{i,p+1} - \mathbf{X}^n_{i,p}}{\|\mathbf{X}_{i,p+1} - \mathbf{X}_{i,p}\|} + S^{\mathrm{link}}(\|\mathbf{X}_{ip} - \mathbf{X}^n_{i,p-1}\| - R)\frac{\mathbf{X}_{i,p-1} - \mathbf{X}^n_{i,p}}{\|\mathbf{X}_{i,p-1} - \mathbf{X}_{i,p}\|}.$$

Letting Δs denote the increment in arclength between consecutive immersed boundary points in their rest configuration, this may be rewritten as

$$\Delta s\Bigg[\Bigg\{S^{\mathrm{link}}(\|\mathbf{X}_{ip} - \mathbf{X}^n_{i,p+1}\| - R)\frac{(\mathbf{X}_{ip} - \mathbf{X}^n_{i,p+1})/\Delta s}{\|(\mathbf{X}_{ip} - \mathbf{X}_{i,p+1})/\Delta s\|} - S^{\mathrm{link}}(\|\mathbf{X}_{ip} - \mathbf{X}^n_{i,p-1}\| - R)\frac{(\mathbf{X}_{i,p} - \mathbf{X}^n_{i,p-1})/\Delta s}{\|(\mathbf{X}_{i,p} - \mathbf{X}_{i,p-1})/\Delta s\|}\Bigg\}\Big/\Delta s\Bigg].$$

This is a discretization of the tension force expression $(\partial(T\mathbf{t})/\partial s)\mathrm{d}s$ in (4.6) in the case of a Hookean tension rule.